Series of Lectures of the University of Applied Science Ruhr West
May, 14th - 15th 2020 | Vol. 8

IEEE WORKSHOP 2020

S2020
ENSORICA

Industrial and Medical Measurement and Sensor Technology
Vehicle Sensor Technology

Abstractbook

UNIVERSITÄT BAYREUTH

ZESS

IM Chapter
IEEE GERMANY SECTION

TECHNISCHE UNIVERSITÄT CHEMNITZ

HRW
HOCHSCHULE RUHR WEST
UNIVERSITY OF APPLIED SCIENCES
INSTITUT MESS- UND SENSORTECHNIK

TTS
Technische Thermodynamik Siegen

UNIVERSITÄT SIEGEN

ITMO UNIVERSITY

UNIVERSITÄT DUISBURG ESSEN

INTRODUCTION

We intend to continue the very successful series of lectures this year. Unfortunately, the event could not take place on May 14th and 15th due to the pandemic. We have decided to cancel the event due to the existing uncertainty concerning the course of the pandemic. All submitted abstracts which were accepted for presentation are published in this abstract book to continue the series of reports this year. As usual, the workshop was organized in collaboration with the Universities of Siegen, Duisburg-Essen, Bayreuth, the Technical University of Chemnitz and the ITMO National Research University of Information Technologies, Mechanics and Optics in St. Petersburg. The event featured for the fourth time an even more international orientation by linking it with the Russian SENSORICA.

Even if the event did not take place, the Abstract Book again offers a platform for knowledge transfer between industry, public and commercial research institutions in the area of measurement technology and offers the opportunity of contacting contributors. We like to thank everybody having contributed to this Abstract Book.

The Organizing Committee:

Prof. Dr. Jörg Himmel, *University of Applied Sciences Ruhr West*
Prof. Dr. Daniel Erni, *University of Duisburg Essen*
Dipl. -Ing. (Univ.) Alice Fischerauer, *University of Bayreuth*
Prof. Dr. Olfa Kanoun, *TU Chemnitz*
Prof. Dr. Thomas Seeger, *University of Siegen*
Prof. Dr. Klaus Thelen, *University of Applied Sciences Ruhr West*

Contents

Low-cost insole foot pressure measurement system
for balance assessment during deadlifting

M. Salmen, R. Gruden

Duale Hochschule Baden-Württemberg, Fakultät Technik, D-70174 Stuttgart, Germany

Abstract –The acquired data from the human feet is used for many different performances, rehabilitations and even security purposes. In weightlifting, the correct execution of the movement is key for safe lifting and completing the repetition. For the deadlift, being a compound movement, where a lot of weight is being lifted and the whole posterior chain of the human body is being used, this becomes even more important. One key aspect is to keep the feet flat on the ground and to equally distribute the pressure during the complete execution. As force platforms prove to be the gold standard in balance assessment and measuring the pressure distribution, they come with a hefty price and require special training. Thus, a lot of research has been made in developing low-cost alternatives for applications such as gait-analysis and early detection of diabetes. This paper presents a low-cost insole foot pressure measurement system designed for balance assessment purposes during the deadlift. The sensors used are force-sensitive-resistors (FSR), which were chosen to be able to measure the weight of the subject and the weight-loaded barbell. Because of the simple implementation and easy-to-use software, the Arduino microcontroller MEGA 2560 was used for data acquisition.

Introduction – As one of the most common powerlifting and bodybuilding exercises, the deadlift is a staple in the weightlifting industry. The name comes from the way the exercise is carried out, with the weight lying on the ground, being *dead* and then lifted up. Because the exercise allows to lift a lot of weight, uses the whole posterior chain of the human body and shows a high activation of the nervous-system, the deadlift is one of the best ways to not only build, but also test strength [1], [2]. But, because the movement uses multiple joints and a lot of weight is often being used, the right execution is essential for safe lifting and to complete the repetition. From keeping your back straight during the exercise, over the right grip/foot stance and width to engaging your core muscles, there are a lot of elements to correctly perform the deadlift. One key aspect is to keep the feet flat on the ground and to equally distribute the pressure during the complete execution. This is directly linked to the center of pressure and balance of the athlete. [1]

In the literature, different approaches for pressure and weight distribution measurement and balance assessment are used. Most systems can be classified into two categories, a platform- or insole-based design. With each system, specific issues arise, which have to be kept in mind when choosing or designing it. Platform based systems often use many sensors in an arrangement of rows and columns, which proves to be higher in resolution. A disadvantage is, that subjects or patients might alter their real walking pattern in order to properly contact their feet to the platform, which can also alter the pressure or force measurement, resulting in faulted data. Insole designs show a lower resolution because of the amount of sensors used, but provide more natural data and better information about the pressure distribution within a shoe. [3]

State of the art – Lei et al. used a force platform to acquire the ground reaction force, which is an important parameter for scientific research but also for weightlifting-training, during snatch weightlifting movements [4]. Beyond weightlifting, plantar pressure measurement has many applications. Corbellini et al. designed a low-cost wearable system for continuous gait analysis [5]. Their approach could deliver crucial information for rehabilitation and training in sport applications, but also to provide early detection for ulceration for neuropathic patients. This is especially important for diabetics, where patients will have a progressive loss of sensation in the lower limbs, often leading to total or partial amputation of the foot [6].

As more of a novel approach, footprint-based person identification has been proposed. Human feet show to have totally unique features just like the fingerprint, while also containing geometric features like the human hand does. Footprint-based identification systems could be integrated in places where its common to take of your shoes, like in bathing centers, praying rooms or in Japanese households for example. Acquired footprint data could have forensic value in comparing it to bare or socked impression of footprints at crime scenes, person verification or linking cases [7].

Methodology – As described by [8], there are certain requirements to the target implementation and the sensor in an insole design. The acquirement systems should be very mobile with limited cabling, as to not interfere with the subject. For the sensor, there are high demands in linearity, temperature sensitivity and the pressure range. These requirements however were made for gait-analyzing systems, for this project there are other requirements important. In weightlifting applications, especially in exercises like the deadlift, which is often

used with a lot of weight, the pressure range is of high importance. This is because the sensor has to be able to measure the weight of the subject and the loaded barbell. Further, to be able to reliable interpret data from multiple repetitions, high repeatability is also required. In applications such as the presented gait-analysis and person identification however, sensor resolution and sensing area are more important. Because of this, a different sensor with different demands is needed. For this application, the sensor FlexiForce A201 from the company Tekscan, Inc. was chosen. With a thickness of about 0.2 mm, high repeatability and force ranges up to 445 N, it allows to measure the needed weight while also fitting in an insole design [9]. The sensor is a force-sensing-resistor based on the piezoresistive effect, meaning that with changes in the applied force, the resistance of the sensors changes.

Results and discussion – The proposed sensor for this project has to be able to measure heavy loads while having high repeatability to be able to reliably interpret data from multiple repetitions of the deadlift. To verify the suitability of the FlexiForce A201 for this project, the measurement setup as seen in figure 1 was used. The FlexiForce sensor is integrated into an operation-amplifier circuit, which outputs a voltage corresponding to the weight applied. For the measurement the sensor was loaded with weights up to 45 kg (measured with a scale) multiple times while the output voltage of the circuit was saved. As seen in figure 2, the system shows a high linearity over the whole applied load on the sensor, while also showing high repeatability. From this, it can be concluded that the FlexiForce A201 is suited for this application.
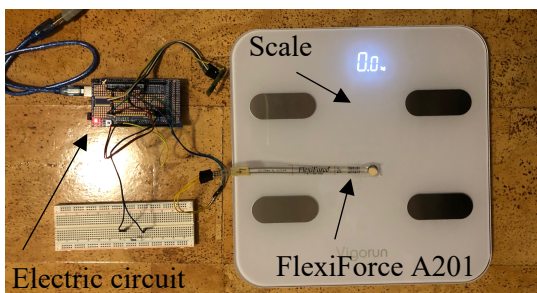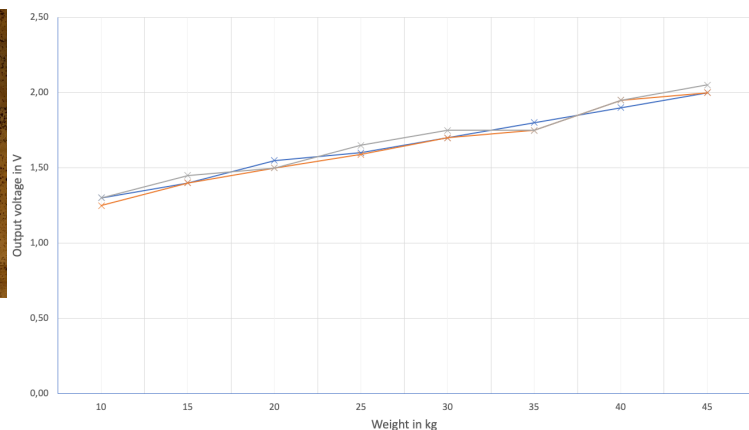

Fig. 1: Measurement setup

Fig. 2: Output voltage over the whole measurable range

Conclusion – This paper presents the work in progress of a low-cost insole foot pressure measurement system for balance assessment during deadlifting. Other approaches in the literature use expensive force platforms in weightlifting applications or sensors with a high resolution in gait analysis or person identification. For a low-cost weightlifting application, the sensor FlexiForce A201 has been proposed. Its high measurable force ranges and high repeatability, verified in this paper, shows its suitability for this project.

References
[1] G. Nuckols, "How to Deadlift: The Definitive Guide," *Stronger by Science*.
[2] R. Patrick, "6 Compound Training Movements Build Serious Mass! | Bodybuilding.com," *2020*, p. 21.
[3] M. N. Orlin and T. G. McPoil, "Plantar Pressure Assessment," *Phys. Ther.*, vol. 80, no. 4, pp. 399–409, Apr. 2000, doi: 10.1093/ptj/80.4.399.
[4] Jianhe Lei, Ming Liu, Jinghua Ma, Quanjun Song, Liankui Qiu, and Yunjian Ge, "Movement Pattern Recognition of Weight Lifter Based on Ground Reaction Force," in *2006 6th World Congress on Intelligent Control and Automation*, Dalian, China, 2006, pp. 10192–10196, doi: 10.1109/WCICA.2006.1713996.
[5] S. Corbellini, C. Ramella, C. Fallauto, M. Pirola, S. Stassi, and G. Canavese, "Low-cost wearable measurement system for continuous real-time pedobarography," in *2015 IEEE International Symposium on Medical Measurements and Applications (MeMeA) Proceedings*, Torino, Italy, 2015, pp. 639–644, doi: 10.1109/MeMeA.2015.7145281.
[6] N. K. Rana, "Application of Force Sensing Resistor (FSR) in Design of Pressure Scanning System for Plantar Pressure Measurement," in *2009 Second International Conference on Computer and Electrical Engineering*, Dubai, UAE, 2009, pp. 678–685, doi: 10.1109/ICCEE.2009.234.
[7] X. Wang, H. Wang, Q. Cheng, N. L. Nankabirwa, and T. Zhang, "Single 2D pressure footprint based person identification," in *2017 IEEE International Joint Conference on Biometrics (IJCB)*, Denver, CO, 2017, pp. 413–419, doi: 10.1109/BTAS.2017.8272725.
[8] A. H. Abdul Razak, A. Zayegh, R. K. Begg, and Y. Wahab, "Foot Plantar Pressure Measurement System: A Review," *Sensors*, vol. 12, no. 7, pp. 9884–9912, Jul. 2012, doi: 10.3390/s120709884.
[9] "Datasheet FlexiForce Standard model A201." Tekscan, Inc., 2019.

Rejection of the Intrinsic Noise for Non-contact Temperature Measurement of an Object in a Closed Cavity

D. Xu[(1)(2)], J. Himmel[(1)], D.Erni[(2)] , K.Thelen[(1)]

(1) Measurement Engineering and Sensor Technology, University of Applied Sciences Ruhr West, 45479 Mülheim a.d. Ruhr, Germany
E-Mail: dawei.xu@hs-ruhrwest.de, joerg.himmel@hs-ruhrwest.de, klaus.thelen@hs-ruhrwest.de
(2) General and Theoretical Electrical Engineering (ATE), Faculty of Engineering, University of Duisburg-Essen,
and CENIDE – Center for Nanointegration Duisburg Essen, 47048 Duisburg, Germany
E-Mail: daniel.erni@uni-duisburg-essen.de

Abstract – A novel and simple method to reject the intrinsic system noise within a non-contact absolute temperature measurement is presented. The absolute radio thermometry usually uses Dicke's radiometer with a known reference temperature source, which has a fixed impedance [1] [2]. This can be applied to the radiometer, if a constant impedance of the antenna exists [3]. However, it is not suitable for the measurement of an object with variable impedance [4]. The impedance of the antenna, including the nearfield coupled object, might change its physical conditions. Moreover, the intrinsic noise of the measurement system depends on it strongly. Using the stochastic method based on a least mean squares algorithm [5] allows a measurement and calculation of the complex noise parameters. As an extension, this method is used to calibrate the intrinsic system temperature and compensate it for the measurement. An improvement of measurements accuracy and a simplification of the measurement procedure is achieved.

Theory – The noise source of an amplifier is modelled by a current and a voltage source, which are partly correlated. The noise characterization of an amplifier can be parametrized with three coefficients, the variances of the noise current source $E\left[\left|\underline{I}_n\right|^2\right]$, the noise voltage source $E\left[\left|\underline{V}_n\right|^2\right]$ and the complex correlation coefficient $\text{Re}\{E[\underline{I}_n \cdot \underline{V}_n{}^*]\}+\text{Im}\{E[\underline{I}_n \cdot \underline{V}_n{}^*]\}$, corresponding to four real numbers [5]. Fig. 1 shows the diagram of the noise model of the measuring amplifier with a coupled input impedance $\underline{Z}_L$ of the measured object, which has the temperature $\underline{T}_L$ proportional to the variance of the available voltage $E\left[\left|V_L\right|^2\right]=4kT_L\Delta f\,\text{Re}\{\underline{Z}_L\}$.
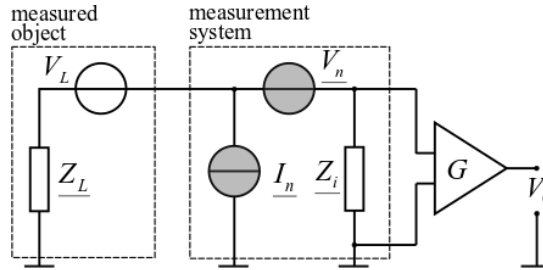
Fig.1: noise model of the measurement system

The output voltage V_o can be measured with a spectrum analyzer and calculated with equation (1).

$$V_o{}^2 = G^2\left|\frac{\underline{Z}_i}{\underline{Z}_i+\overline{\underline{Z}}_L}\right|^2\left(\begin{array}{c}4kT_L\Delta f\,\text{Re}\{\underline{Z}_L\}+E\left[\left|\underline{V}_n\right|^2\right]+E\left[\left|\underline{I}_n\right|^2\cdot\left|\underline{Z}_L\right|^2\right]-\\-2\,\text{Re}\{\underline{Z}_L\}\cdot\text{Re}\{E[\underline{I}_n\cdot\underline{V}_n{}^*]\}-2\,\text{Im}\{\underline{Z}_L\}\cdot\text{Im}\{E[\underline{I}_n\cdot\underline{V}_n{}^*]\}\end{array}\right) \tag{1}$$

where k is the Boltzmann constant, Δf the measurement bandwidth and G the gain of the amplifier. For impedance matching we have to measure the input impedance of the amplifier $\underline{Z}_i$ and the coupled impedance $\underline{Z}_L$ using a network analyzer previously. As the three noise coefficients and the coupled impedance $\underline{Z}_L$ are independent of each other, the characterization of the noise coefficient is carried out by using a set of arbitrary but known input impedances at known temperatures. In order to obtain the four mentioned numbers a calibration with at least four arbitrary impedances needs to take place. In our case, we used 10 different

calibration impedances covering a large range of the complex Z-plane. For the calculation of the noise coefficients a least mean square algorithm was used according to the method described in [5]. This leads to more accurate values of the noise coefficients as the dependence of the noise sources from the input impedance is better represented. Using this method, the system noise temperature is determined by:

$$T_{sys} = \frac{E\left[\left|\underline{V}_n\right|^2\right] + E\left[\left|\underline{I}_n\right|^2 \cdot \left|\underline{Z}_L\right|^2\right] - 2\,\mathrm{Re}\{\underline{Z}_L\}\,\mathrm{Re}\{E\left[\underline{I}_n \cdot \underline{V}_n^*\right]\} - 2\,\mathrm{Im}\{\underline{Z}_L\}\,\mathrm{Im}\{E\left[\underline{I}_n \cdot \underline{V}_n^*\right]\}}{4k\Delta f\,\mathrm{Re}\{\underline{Z}_L\}} \tag{2}$$

The temperature of the object can be calculated by subtracting system noise temperature from the total noise temperature of the spectrum analyzer:

$$T_{obj} = \frac{P_m \cdot Z_0}{4k_B\Delta f\,\mathrm{Re}\{\underline{Z}_{ant}\} \cdot G^2 \cdot \left|\dfrac{\underline{Z}_i}{\underline{Z}_i + \underline{Z}_L}\right|^2} - T_{sys} \tag{3}$$

Experiment and result – The calibration of the amplifier for the impedance measurement was carried out first. The 10 known impedance terminations, which are made of different lumped elements, were hooked on the input of the amplifier at known room temperature. Afterwards an object consisting of a thermally controlled hose with salt water was set to 5 different temperatures. Fig. 2 (a) shows the results of the calculated temperature according to (3). Fig. 2 (b) shows the average temperature in the marked range of 1.69–1.76 GHz.
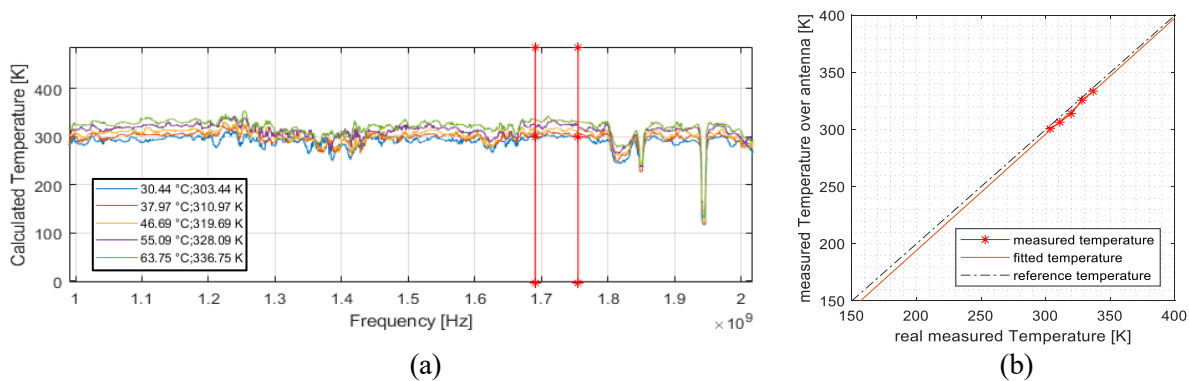

(a)   (b)

Fig.2: Calculated temperatures of the measured salt water

The offset of the fitted temperature line shows a low deviation in comparison to the measured reference temperature, describing a correct evaluation of the intrinsic noise level of the system. From Fig. 2 (a) it can be seen that different frequency ranges show slightly different temperature offsets, indicating that a fully compensation of the system noise is not possible for all input impedances.

Conclusion – Compared to the traditional characterization of the intrinsic noise, this method allows a system noise calibration without disassembling the measurement setup at any time between the temperature measurements. The accuracy for the temperature measurement will improve, if more calibration impedances are in use. An automated calibration procedure can be realized using e.g. a mechanical multiplexer. In combination with an in-situ measurement of the object impedance, the system performance could be significantly enhanced.

References

[1] W. Susek, "Thermal microwave radiation for subsurface absolute temperature measurement," *Acta Physica Polonica-Series A General Physics*, vol. 118, no. 6, p. 1246, 2010.

[2] W. Park and J. Jeong, "Total power radiometer for medical sensor applications using matched and mismatched noise sources," *Sensors*, vol. 17, no. 9, p. 2105, 2017.

[3] Ø. Klemetsen, Y. Birkelund, S. K. Jacobsen, P. F. Maccarini, and P. R. Stauffer, "Design of medical radiometer front-end for improved performance," *Progress in electromagnetics research B. Pier B*, vol. 27, p. 289, 2011.

[4] D. Xu, D. Rüter, J. Himmel, D. Erni, and K. Thelen, "Non-contact radiative temperature measurement of an object in a closed cavity," in *Proceedings of the 47th European Microwave Conference*, 2017, pp. 872–875.

[5] B. Lehmeyer, M. T. Ivrlac, and J. A. Nossek, "LNA noise parameter measurement," in *Circuit Theory and Design (ECCTD), 2015 European Conference on*. IEEE, 2015, pp. 1–4.

Evaluation of Crosstalk in SOI technologies for Sensor Applications using optimized Measurement Methods

B. Bieske[1], A.Ott[2], M. Frey[2]

(1) IMMS GmbH, D-98693 Ilmenau, Germany
(2) Melexis GmbH, D-99099 Erfurt, Germany
E-Mail: bjoern.bieske@imms.de; Web: www.imms.de;

Abstract – Crosstalk can reduce the performance of RF, analog, mixed-signal and digital integrated circuits (ICs). Different measurement parameter sets to characterize the crosstalk were evaluated for SOI (Silicon-On-Insulator) technologies. Based on these results the designer can choose and combine layout options to improve the isolation between building blocks of the IC. Different technological parameters were compared. The efficiency of isolation measures depends on the desired frequency range. The S-parameters of several test structures were measured in the range from 10 MHz to 4 GHz using a vector network analyzer.

Introduction – Increasing integration densities are leading to more and more complex systems on a chip (SoC). In automotive ICs we can find a combination of drivers for high voltages or currents with sensor components processing low voltage signals. Insufficient isolation between parts of analog, mixed-signal or RF-ICs is a severe problem which has to be considered during the whole design process of the system. Sensor data can be corrupted by crosstalk interferences generated by other components. SOI technologies offer advantages in isolation compared to standard CMOS technologies due to their isolated substrate [1].

Test Structures– The test structures have to be suitable for reproducible crosstalk measurements in the GHz range. To extract the different influences on the isolation behavior the following layout parameters of the test structures are modified independently (see Fig. 1):
- Substrate resistivity of SOI technology [2]
- Distance of the pads (grey, pitch = 200..800 μm)
- Area of trench islands (square = 100..200 μm)
- Trench layout (black, single / double trench,)
- Contact type: „Shielding well", with / without bias
- Ground / guard rings (blue)
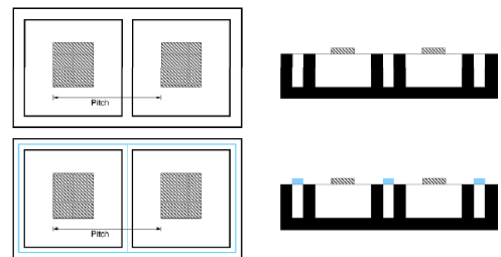- Handle wafer contact (HWC): Floating or grounded

Fig.1: Layout variants of test structures in top and cross section view

Optimized measurement setup – In the past the measurement parameters were derived mainly from the available measurement equipment. We tried the opposite way: Select the measurement devices based on required measurement parameters for optimal results. Indicative RF-measurements were done in the range from 50 MHz to 20 GHz using a network analyzer HP8510 and measurement probes ACP40. The first result was: Most interesting are the shapes of the different traces below 1 GHz. Many automotive and sensor applications are running in this frequency range. We need a high dynamic range for those measurements.

The frequency range for evaluation was newly defined from 10 MHz to 4 GHz requiring a dynamic range of up to 100 dB. A shielded chamber was used to avoid influences from a noisy environment. The final measurements were done using a network analyzer ZVA8 by Rohde & Schwarz fulfilling all requirements in the whole frequency range to provide reliable measurement results. The step of isolation measurements during S-parameter calibration was skipped. Otherwise crosstalk effects could not be measured.

Measurement results and analysis – Based on a matrix of the changed parameters a set of 22 test structures were manufactured and characterized on wafer [2]. The measurements were done on two SOI wafers differing in their substrate resistivity (medium resistivity MR, high resistivity HR). We evaluated five locations distributed across the wafer. In summary 350 data sets were analyzed and processed. Large differences of crosstalk were shown between high and medium/low substrate resistivity SOI technologies.

The maximum of differences was shifted from 1 GHz to around 100 MHz compared to literature data [1][3]. The optimization of measurement parameters towards lower frequencies has paid off and delivered better results to compare the possibilities for crosstalk reduction in sensor applications. The quantity of reduction of crosstalk proved to be strongly dependent on frequency for the different kinds of layout options. To distinguish between the effects, only single parameters will be compared in data analysis. The corresponding traces of high and medium/low resistivity are plotted together into the diagrams to compare their performance and frequency response more easily (Fig. 2).

Evaluation of Crosstalk Reduction – With the optimization of measurement environment and parameters significant differences of crosstalk could be observed in the frequency range around 100 MHz. In general, the high resistivity substrate SOI of wafer W14 shows up to 20 dB less crosstalk at these frequencies (Fig. 2) compared to wafer W03 (MR) where the area of island is varied. At high frequencies above 1 GHz more double trenches and guard ring improve the isolation. Finally we can extract three general rules for isolation measures to reduce crosstalk:

- At frequencies above 1 GHz larger pitch and trenches with guard rings reduce crosstalk essentially.
- At frequencies below 100 MHz biased nWells and HWC grounding can provide additional isolation.
- Around 100 MHz high resistivity SOI substrates show better performance than lower resistive ones.

Now it is up to the designer to determine which isolation between building blocks of a SoC is needed for proper functionality. With the help of the presented data sets he can decide which layout options or combinations of them will be applied in the system on a chip. The choice can be different for any application and depends strongly on the frequency range of the signals and levels used in the integrated circuit.

Conclusion – The influence of the technological parameter substrate resistivity on crosstalk has been evaluated. The measurement setup was optimized towards a lower frequency range and a higher dynamic range. A set of isolation measures was characterized by S-parameter measurements (VNA ZVA8). Since the parasitics are a part of the cross talking structure the deembedding procedure in S-parameter analysis was omitted. They can be used during the design process as building block system to minimize crosstalk. The efficiency of a single isolation measure depends on its combination with others and their parameters and on the desired frequency range.
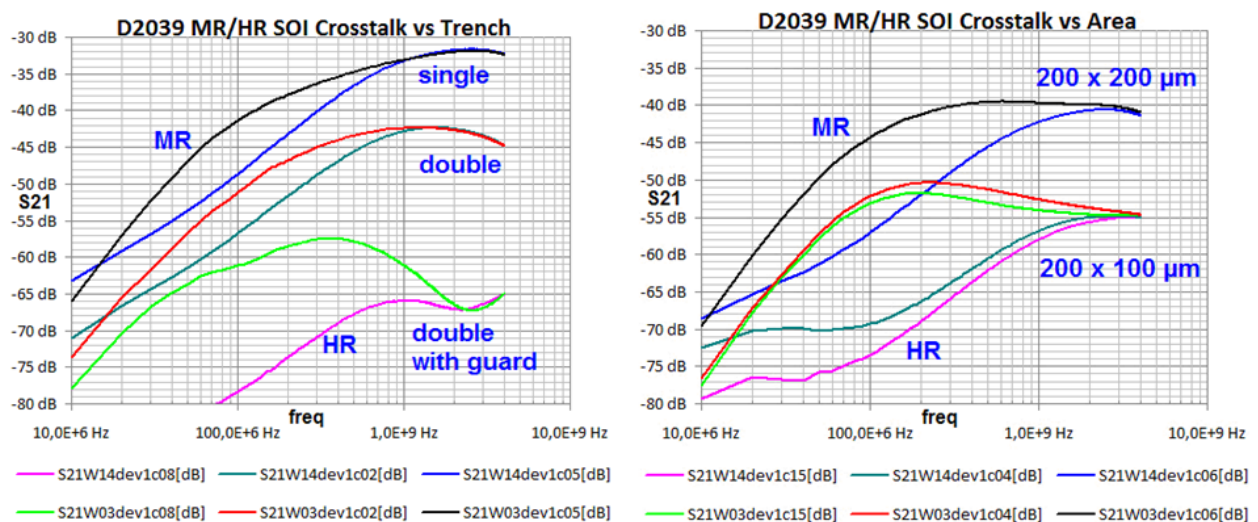

Fig.2: Comparing crosstalk in medium and high resistive SOI varying trenches (left) and island areas (right).

The simple equivalent circuit topology shows the main contributions to crosstalk only. It has also been found that crosstalk depends on both the geometry and the impedance of application elements. The data processing was done without any deembedding. The deembedding procedure can be inserted into the calculation later at any time if required. In general the measured data meet the expectations created by earlier measurements and data of literature sources. The visualization of diagrams was done using MS Excel. The raw data traces show a smooth shape without any peaks or outliers. The suitability of the measurement setup could be confirmed.

References

[1]   J.-P. Raskin, A. Viviani, D. Flandre, and J.-P. Colinge, "Substrate crosstalk reduction using SOI technology", IEEE Trans. Electron Devices, vol. 44, no. 12, pp. 2252–2261, Dec. 1997.

[2]   J. Ankarcrona, L. Vestling, K.-H. Eklund, and J. Olsson, " Low Resistivity SOI for Substrate Crosstalk Reduction", IEEE Trans. Electron Devices, vol. 52, no. 8, august 2005, p. 1920-1922.

[3]   A. Ott, „Validation test chips XP018 / XT018 TC947/948 – Cross-talk" Präsentation Melexis.

[4]   V. Issakov ; J. Rimmelspacher ; A. Werthof ; A. Hagelauer ; R. Weigel, „Experimental study on substrate coupling in bulk silicon and RF-SOI CMOS up to 110 GHz", 2017 IEEE MTT-S International Microwave Symposium (IMS).

[5]   T. Hashimoto ; H. Satoh ; H. Fujiwara ; M. Arai, „A Study on Suppressing Crosstalk Through a Thick SOI Substrate and Deep Trench Isolation", IEEE Journal of the Electron Devices Society, 2013, Volume: 1, Issue: 7. Page s: 155 – 161.

Flexible PXI-Plattform for enhanced Evaluation and Test of RF- and UHF-RFID Sensor Systems

B. Bieske[1], T. Reinhold[1], J. Tan[1]

(1) IMMS GmbH, D-98693 Ilmenau, Germany
E-Mail: bjoern.bieske@imms.de; Web: www.imms.de;

Abstract – RFID (Radio Frequency Identification) is a widely used technology for contactless identification of devices in many fields. The combination of wireless energy transfer and data transmission with low power sensor systems created a variety of new applications. The evaluation of these systems leads to enhanced requirements to the measurement equipment. Based on standard equipment available in the lab and special RFID readers we developed a complex measurement platform using PXI instruments. With the help of these PXI-modules complex measurement sequences can be realized to characterize and test RFID transponders with sensor interfaces.

RFID-Basics – The default application scenario for RFID is the identification of tagged objects. The RFID system consists of a reader and the transponder tag generating a unique RFID code on request [1]. The reader establishes the communication with the tag. Active tags have their own power supply. The power supplies of passive tags are realized with the help of the (electro-)magnetic field generated by the reader. These passive tags lead to an increased use of RFID technology in transportation, logistics, access control, sports and payments.

The decreased costs, increased performance and reliability and the global standardization of RFID-systems were the reasons for their worldwide distribution (main standard: ISO/IEC 18000).Telemetry applications are using RFID to transmit data. In combination with remote power supply autonomous sensor applications without batteries can be implemented.

One application of RF RFID running at 13.56 MHz is well known as NFC (Near Field Communication, standard ISO 18092) and used for data acquisition or payment transactions over short distances. The energy and data transmission is based on magnetic coupling between two coils. The maximum distance is limited to a few centimeters and can be estimated as the diameter of the coils.

In contrast, the energy and data transmission of UHF-RFID systems are based on radiated electromagnetic fields using antennas. Depending on geometry, radiation pattern and gain of these antennas a coverage of several meters can be achieved. The available power at the tag is in the range of microwatts and sufficient to supply ultra low power sensors (ULPs). The communication is realized via a memory area within the RFID tag. The digital part of the tag interprets the RFID command and controls the operation of the connected sensor. The sensor stores the measured data in the tag memory. The stored values can be read out by the RFID reader.

Evaluation of RFID sensor tags –Dedicated test systems are offered for characterization and test of RFID components. They assume a fully functional RFID device to measure its parameters. Usually this condition is not fulfilled during the design process of a RFID system. This fact created the need to evaluate the individual parts of the system separately.
The check of functionality can be split into the following parts:
- Energy transmission, energy harvesting, power supply of the tag
- Data transmission to the tag (amplitude modulation ASK with different modulation depth)
- Answer of the tag (backscatter modulation for UHF, load modulation for RF)
- Functionality of the tag (data storage, digital part, interface to sensors, power management)

These function blocks are independent from each other but they are building on each other for a tag working correctly. Based on the experiences with RF-RFID Systems the evaluation of UHF-RFID tag ASICs with sensor interface D1028A and D1030A developed by IMMS [2] will be explained.

As the first step the energy transfer was measured using signal generators and dipole antennas over short distances. A demodulator for RFID commands was set up using a UHF detector for AM signals. So the data transmission to the tag could be analyzed in the baseband. Next the digital interface to the sensor was checked for correct I2C protocol timings.

Complete characterization of RFID tags can only be done using complex measurement setups. These can be realized by PXI modules arranged to a flexible measurement platform which was implemented at IMMS. Standard compliant measurements defined conformance and performance tests were done based on LabVIEW control software by CISC [3].

Conformance means the check of the protocols for RFID and performance tests include all parameters of the tag like maximum read, backscatter and write range, frequency response, tag spectrum, interference immunity

etc. Two separated antennas were used for transmitting and receiving of RFID signals in the UHF range. Due to the further decoupling of antennas by polarization a reasonable carrier cancellation could be achieved leading to a high sensitivity of the system.

Measurement results – The functionality of UHF-RFID ASIC D1028A is guaranteed at a minimum supply voltage of 1.65 Volts. The antenna matching of the initial version was measured and then optimized for better performance. The resonance frequency of input circuit had to be tuned to the desired frequency of 868 MHz. Additionally performance tests had shown that the maximum sensitivity of the initial tag was at 830 MHz (Fig. 2). Table 1 shows the improvement in power supply of the optimized tags. The frequency response was shifted to the 868 MHz (Europe) and 920 MHz (USA) Band (Fig. 3).

Conformance tests were done at the same six sample tags. The ID number was read correctly according to the transmitted RFID commands. The communication to the tags was verified according to the RFID standards. In the waterfall diagram the sidebands of the tag response were verified.

TABLE I. VERSORGUNGSSPANNUNG DER RFID-TAGS BEI 870 MHZ

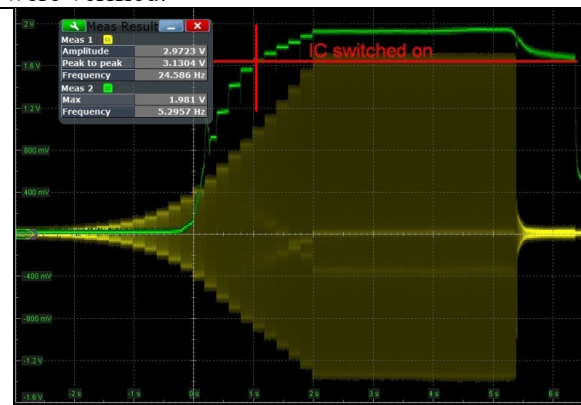| Tag	Versorgungsspannung ungeregelt vs. Sendeleistung			
	Leistung an Sendeantenne [dBm]	*+7*	*+10*	*+13*
Nr.	*Rohspannung Vunreg in V*			
1	Board 2 Initialversion (Fig.8)	0,69	1,12	1,47
2	Board 2 Antenne optimiert	1,36	1,51	**1,66**
3	Board 3 Initialversion	0,65	1,09	1,41
4	Board 4 mit L=8,2 nH optimiert	1,36	1,6	**1,85**
5	Board 5 mit L=8,2 nH optimiert	1,25	1,65	**1,8**
6	Board 6 mit l=6,8 nH optimiert	1,13	1,48	**1,75**

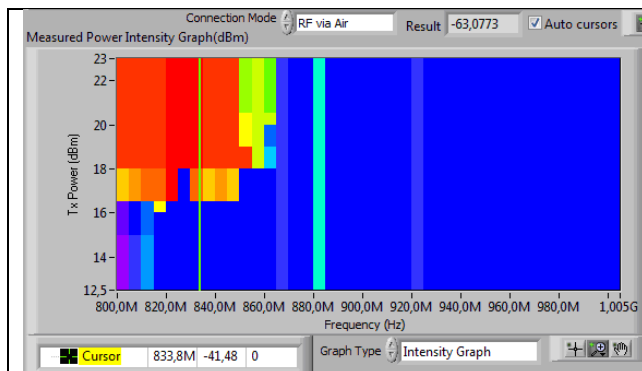*Fig.1: RF-field (yellow) and supply voltage(green)*

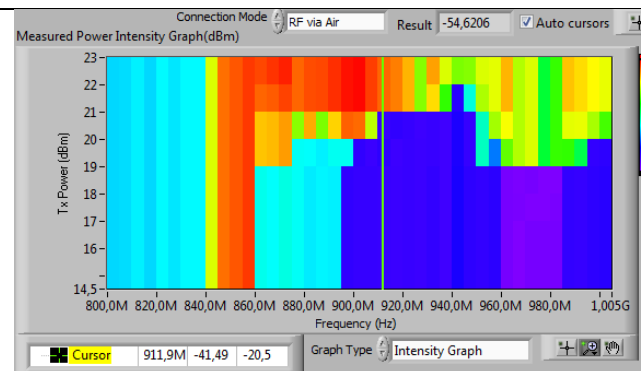*Fig.2: Frequency response of tag 1: resonance to low*

Fig.3: Frequency response of tag 2: optimized antenna circuit

Conclusion –The functionality of RFID-tags with sensor interface was confirmed step by step. The single measurements were done with the help of a PXI measurement platform implemented by IMMS. We have gained essential insights for the redesign process of ASICs. Complex measurements were done using LabVIEW to certify that the tags meet the specifications of conformance and performance tests [3].

These tests were done using flexible configurable PXI modules establishing a RF measurement setup for RF and UHF-RFID applications. Due to the use of SDR (software defined radio) based modules for signal generation and analysis the needed space could be reduced from ten to seven slots in the PXI rack compared to the classic approach with digitizer and waveform generator. The works are a part of the project "RoMulus" funded by BMBF (FKZ: 16ES0362) within the program IKT 2020.

References

[1] B. Lenk, RFID Das Praxisbuch für Anwender, Lenk, 2015.
[2] Tan, et al. „An RFID to I2C Bridge IC with Supply Interference Reduction for Flexible RFID Sensor Applications" 13th Annual, 2019 IEEE Int. Conference on RFID, 2-4 April 2019, Phoenix, Arizona, USA.
[3] https://www.cisc.at/products/rfid-meets/ (18.12.2019)

Underwater laser strobe visual system in turbulent and turbid media.

A L.V.Grigoryev[(1)] , Y.C.Mashek[(2)] A.V.Sandulenko[(3)]

(1) ITMO University, Kroverksy Pr.,49, 197101 St. Petersburg, Russia
(2) Saint Petersburg University, Universitetskaya Emb. 7, 199034 St. Petersburg, Russia
(3)Research and Technological Institute of Optical Material Science,Babyshkina Str., 36/1, 192171 St. Petersburg, Russia
E-mail:lvgrogoryev@itmo.ru

Abstract

The article presents the results of the research and development of a laser strobe underwater television system for autonomous underwater vehicles (AUVs) and remotely operated vehicles (ROVs). Gated laser vision systems are designed for use in the foreseeable systems of technical vision of underwater robotic platforms for various purposes, which operate in a very turbid (muddy water) environment. The use of such vision systems can significantly expand the use of underwater robotic systems for inspection of underwater pipelines, cables, bridge supports and other underwater objects.

Introduction

The futility of increasing the power of continuous lighting systems to increase the viewing range of TV systems in highly cloudy environments necessitates the use of dynamic target illumination. If the shutter of the TV camera has an open time comparable to the duration of the light packet and the delay in opening corresponds to the required range, then the target detection range increases by approximately the same amount as the object is visible in the suspension under the condition of spurious illumination by backscattering luminescence. This work presents the result of creating a gated complex of a laser vision system with dynamic laser illumination of a target in the absence of unambiguous data on the decay time of the fluorescence of suspensions in which the system will have to work.

For calculations and subsequent design, the following initial data were adopted: Maximum distance to the facility –15 m, the field of view of the system at this distance is a circle with a diameter of 5 m, the CCD camera used has an amplification section with a MEC – EOP, the shutter open state is 3 ns, the minimum illumination of the object is 5×10^{-5} lux, during the calculations, the values of the relative aperture of the camera lens A = 0.7, the coefficient of electron-optical magnification k = 4, the pixel size of the camera 10x 10 μm^2. A DPSS laser with the following characteristics was selected into the optical sounding channel: output energy at the second harmonic (wavelength 532 nm) at least 30 mJ, pulse duration at half height - no more than 2 ns, average power within the pulse 300 kW. Power consumption no more 38 W, repetition frequency 100-1200 Hz, synchronization and control via RS-485 interface The value of the visibility function for 532 nm was taken equal to 0.5.

When calculating the range of the laser gated vision system, the worst case scenario was chosen, corresponding to the conditions of the Baltic Sea. For a wavelength of 532 nm, the attenuation coefficient was taken equal to $0.1 \ m^{-1}$[1,2]. The general scheme of laser strobe TV underwater system is presented in Figure 1.
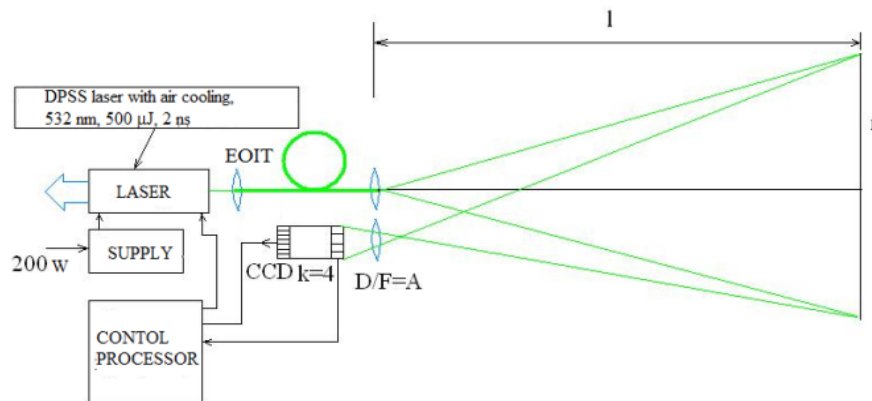

Fig. 1: The general scheme of laser strobe TV underwater system.

Result and discussion

Tests of the model of the proposed system were carried out at the sea stand. The total signal attenuation at a distance of 15 m was 120 - 130 times, the laser energy was 30 mJ, the mode was monopulse. The gated camera had the parameters indicated above. The object was the "Seki" disk (a round white disk 0.4 m in diameter) on which two black marks were applied to assess the spatial resolution of the system. The image of the disk observed by the system with the above parameters is presented in Fig. 2. The analysis of the obtained image gives reason to assert that even under such severe conditions of attenuation the test system allows not only to detect objects of size 0.3-0.4 m (Seki disk), but also to distinguish significantly smaller details on it.
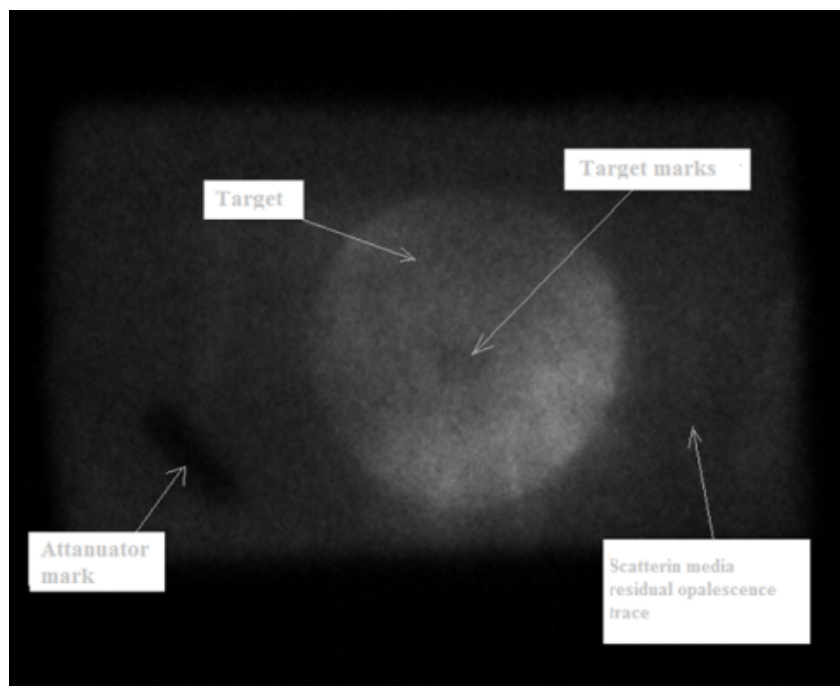

Fig. 2: The result of field testing of a laser gated TV system.
Target detection in the form of a "Seki" disk and details on it.

Conclusion We note that the considered and tested version of the system is based on the parameters of a commercially available DPSS laser, the characteristics of which can be significantly improved during its refinement. It should also be noted that a significant gain in the sensitivity of the system and its resistance to parasitic signals of the reverse fluorescence of suspensions can be obtained through subsequent digital image processing (wavelet, adaptive autocorrelation and storage schemes).

References

[1] D.B.Ingham, X.Wen, Separating inviscid flows, J. Act. Mech., **86**, pp. 1-14,1991

[2] G.N.Pologij , An Extension of the Theory of the Analytic Functions of the Complex variables, Kiev, Kiev State University, 424 pp. (in Russian),1965

Two axis MEMS accelerometer with SAW

L.V.Grigoryev[1,2] , A.A.Semenov[2]

(1)ITMO University, Kroverksy Pr.,49, 197101 St. Petersburg, Russia
(2)Saint Petersburg government Electro technical University "LETI", Prof.Popova Pr. 7, 197034 St. Petersburg, Russia
E-mail: lvgrigoryev@itmo.ru

Abstract

The article presents the results of a designed and created two axis micro accelerometer using MEMS technology. The results of the creation of a MEMS accelerometer on the surface console sensor where a surface acoustic wave propagates, and investigation of its sensitivity and nonlinear properties in the commercial temperature range are presented in this paper. This accelerometer was used in navigation and control systems of underwater robotic platforms: autonomous underwater vehicles (AUVs) and remotely operated vehicles (ROVs).

Introduction – Accelerometers with surface acoustic waves (SAW) [1-3] represent a promising class of phase- and especially frequency-type micro accelerometers that make it possible to realize a high level of constructive integration, provide high resistance to external disturbances, the possibility of a significant reduction in the number of parts and connections between them. They provide the ability to overlap without compensation for a wide operating range (up to 100 g) with the frequency form of the output signal. Micro accelerometers with SAW, as a rule, are created on a single substrate with two SAW-converters. The placement of SAW-converters in two parallel planes of the moving part of the micromechanical sensor and their subsequent differential inclusion allows compensating for the infelicities due to thermal effects in the moving part of the micromechanical sensor. However, such a topology for placing SAW-converters on the surface of a mobile sensor leads to a significant complication of the technology for creating a micro accelerometer. This article presents the results of the investigation of micro accelerometer characteristics in which two SAW-converters are located in the one plane and one surface. This provides simplicity in the technology of creating ultrasonic converters on the surface of the console of micromechanical sensors. One of the SAW-converters is placed in the zone free from deformation.

Experimental installation– The MEMS sensor of the accelerometer was created using planar silicon technology on the $Si-SiO_2-ZnO$ structure. Initially, a thin film of piezo semiconductor ZnO was deposited on the surface of the $Si-SiO_2$ structure. The zinc oxide thin film was formed by reactive magnetron sputtering of a metal target. The topology of the sensor element of the MEMS accelerometer (MEMS sensor console present at Fig.1) was formed using a micro-dimensional laser treatment, using photon-stimulated silicon surface etching [4].
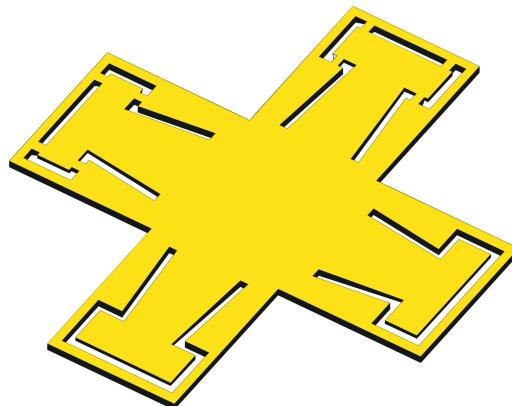
Fig. 1: Structure scheme of two axis micro accelerometer with SAW.

Result and discussion

The modern methods of thin film the technologies used in the creation of SAW resonators show that the limiting accuracy of the tuning of each individual resonator can vary from ± 50 kHz to ± 115 kHz in the used frequency band lying near frequency of 480 MHz. MEMS accelerometer characteristics when acceleration causes bending of the cantilever beam outwards is presented in Fig. 2.

Fig. 2: The output dependence of the frequency shift on acceleration in a micro accelerometer

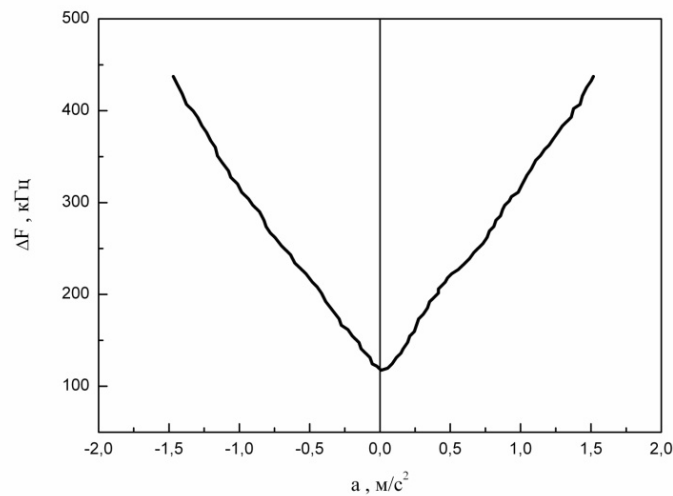The performance of the SAW delay lines is directly influenced by the accuracy of manufacturing the topology of the interdigital electrodes. Also influence on the characteristics of the MEMS sensor has the quality of the surface of the thin piezosemiconductor film, causing different propagation velocities of the wave (SAW).

The operating frequency of the SAW accelerometer was 460 MHz, the frequency tuning was 370 kHz. As a result of the investigations, the MEMS accelerometer had the following characteristics: sensitivity 340 $(Hz/m/s^2)$, acceleration ranges -1,8…+1.8 (m/s^2), nonlinearity of the output characteristic was near 2%, operating temperature range 0 – 60 ^oC.

Conclusion

The presented two axis SAW micro accelerometer can be used to create inertial motion control systems for UAVs or underwater ROVs/AUVs.

References

[1]   M. Norgia, S.Donati, Hybrid Opto-Mechanical Gyroscope with Injection-Interferometer Readout, *Electronics Letters*,37(**12**), pp. 756–758,2001

[2]   J.R. Fountain, Silicon IMU for Missile and Munitions Applications, *Advances in Navigation Sensors and Integration Technology, NATO RTO Lecture Series-232*, p. 10,2003

[3]   J.Filipiak, L.Solars, G.Steczko, *Surface acoustic wave (SAW) vibration sensors*, **11**, pp.11809-11832,2011

[4]   G. Reksten, W.Holber, R.Osgood, Laser controlled plasma etching, *J.Vac.Sci.Tech.*,A2(**2**), Pt.1,1994

Changing the sensory properties of the cell membrane in modelling impacts of free radicals

A. Mamykin[(1)], A. Rassadina[(1,2)], K. Frolova[(2)]

(1)   Saint-Petersburg Electrotechnical University "LETI", Institute of Basic Engineering Education, Department of Physics, RF-197376, Russia
(2)   ITMO University, Faculty of Control Systems and Robotics, RF-197101, Saint-Petersburg, Russia
E-Mail: alexmamykin@yandex.ru; Web: http://www.physicsleti.ru

Abstract – This paper presents the study of cellular membrane lifetime by the help of a physical model. The cell lifetime in the time of homeostasis, free radicals concentration jump and chronically increased concentration of free radicals were investigated.

Introduction – The cause of many socially significant diseases (for example cancer or Alzheimer's disease) are free radicals [1], [2]. In the work, all diseases of a free-radical nature are divided into two groups and examined on the example of exophtalm and polymyosite. The cause of exophtalm is a short-term increase jump of radicals' concentration. Polymyosite is connected to the level of free radicals chronic excess in the body.

Fig. 1: The principle of the program: 0, 0.3 – neutral centers; 0.8 - positive center; -1, -2 – cells in the process of oxidation; -4 - dead cells; -3 - cluster center

Method – The effect of free radicals on the energetically heterogeneous surface of the cell membrane is considered. This surface is a neutral surface interspersed with positive centers (integral proteins). As part of the study, a program that simulates the interaction of free radicals and cell membranes was developed. The surface of the membrane was presented in the form of a matrix in which three types of centers were reflected: neutral, active, and dead (Fig. 1). When negatively charged particles (free radicals) hit the active centers, a reversible oxidation process began. If the center was finally oxidized, it became the dead center. When negatively charged particles hit it, a cluster of dead cells began to form. Using the program, we studied three main models that reflect the dynamics of the process: dynamic equilibrium (homeostasis), exophtalm and polymyosite.

Results – The results of the program were graphs of the cell lifetime depending on time (Fig.2), (Fig.3), (Fig. 4). Even in a state of dynamic equilibrium, the cell's lifetime was limited. When a shock dose of radicals was introduced, the rate of cell death increased sharply, but then returned to its original state. With a chronically increased amount of radicals in the body, the shape of the curve remained the same as in homeostasis, but the death rate was larger [3].
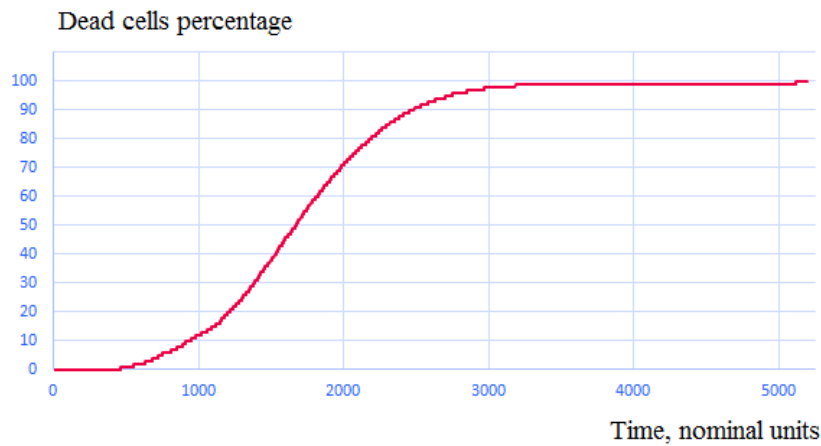
Fig. 2: Determination of homeostasis
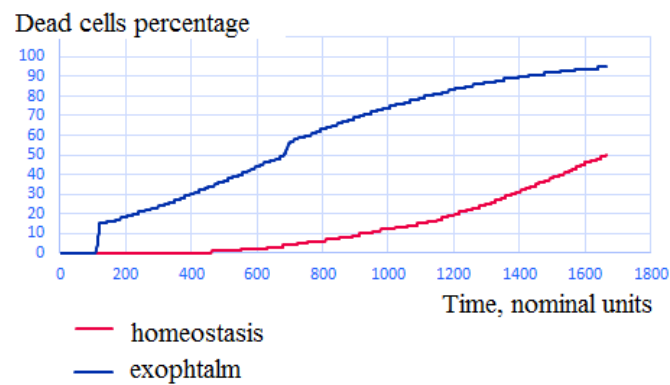
Fig. 3: Comparison of homeostasis and exophtalm
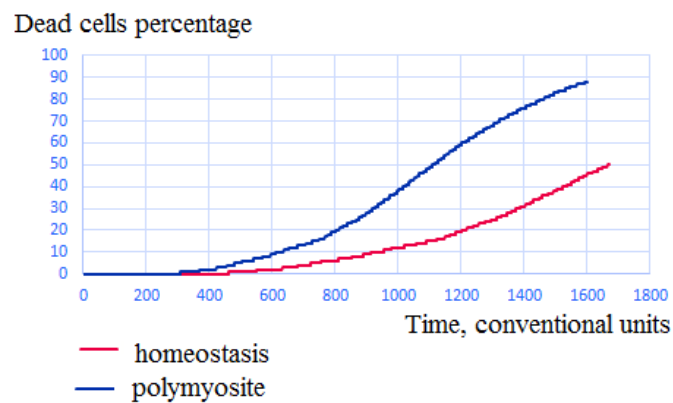
Fig. 4: Comparison of homeostasis and polymyosite

References

[1]   M.Valko, C.J.Rhodes, J.Moncol, M.Izakovic, M.Mazura "Free radicals, metals and antioxidants in oxidative stress-induced cancer", Chemico-Biological Interactions, vol. 160, is. 1, pp 1-40, 2006

[2]   M.A. Smith, G. Perry "Free radical damage, iron, and Alzheimer's disease", Journal of the Neurological Sciences, vol. 134, pp 92-94, 1995

[3]   M.V. Listov, A.I. Mamykin "Organism as a biosystem, adapted to the using of the energy of quantized electron transport via free radicals", Herald of the Russian Military Medical Academy, 2016, no. 4 (56), pp. 200−204 (in Russian)

Experimental results to identify the air flow formation in a 3D nose model during the breath simulation

G. Lukjanov[1,2], A. Rassadina[1,2], A. Kasatkin[1], R. Neronov[3]

(3)   ITMO University, Faculty of Control Systems and Robotics, RF-197101, Saint-Petersburg, the Russian Federation
(4)   Saint-Petersburg Electrotechnical University "LETI", Faculty of Radio Engineering and Telecommunications, Department of Microradioelectronics and Technology of Radioequipment, RF-197376, the Russian Federation
(3) JSC "Modern Medical Technologies", Otolaryngology Department, RF-190121, Saint-Petersburg, the Russian Federation
E-Mail: gen-lukjanow@yandex.ru; Web: https://en.itmo.ru/en/

Abstract – The physiology of respiration is being studied depending on the shape of the nasal cavity. A method for measuring respiration parameters directly in a solid-state three-dimensional model with a sensor system is presented. The signals from the pressure sensors in the solid-state three-dimensional model are taken as the basis for digital modeling of air movement along the nasal passages.

Introduction – Studying of the air flow moving in the nasal cavities is a sophisticated problem [1], [2]. Nasal cavity has a branched shape of irregular cross-section. Turbinate bones divide the cavity into four nasal passages. The complex internal structure of the nasal cavity makes study of breathing difficult. One of the main ways of breathing research is to apply experimental studies at the full-scale models of the nose. The sensor system based on pressure sensors has been developed for this study.
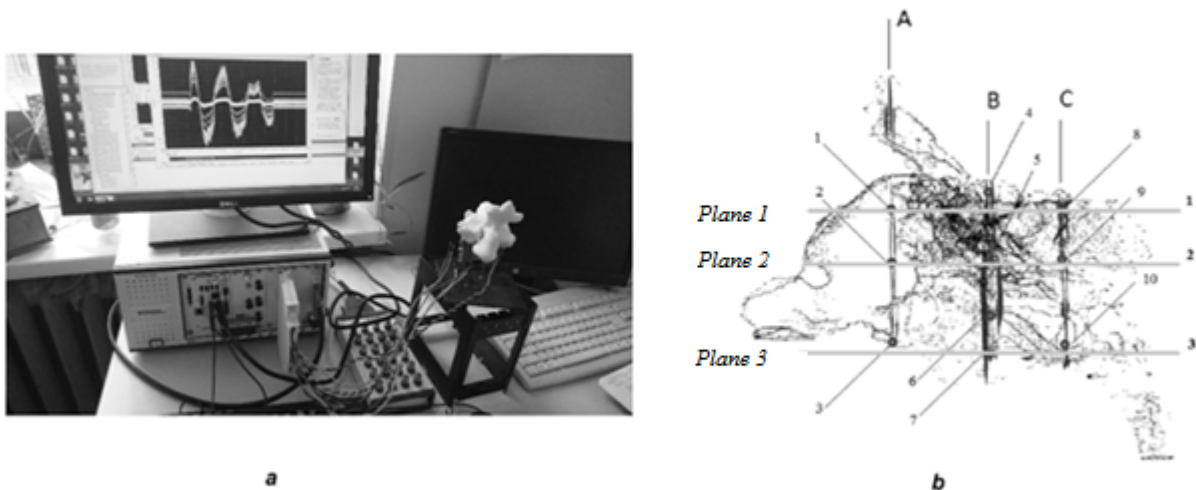

Fig.1: Sensor system for breath parameters measurement: (a) general view of the sensor system with measurement results; (b) places of location thin shunt tubes for measuring of pressure at the 3D model

Materials and Methods – The solid-state 3D model, the sensor system and a data acquisition system has been used as the base of the experiment. The model was developed by 3D printing with a 1:1 scale. The models completely reflect the nasal cavity including all the nasal sinuses that are open into the nasal cavity. Imitation of breathing was performed through a tube that was fixed to the nasopharynx area of the model. Experiments were carried out by inhaling and exhaling successivly through the tube during the simulation of respiration. Thus this simulation can be considered as approximating human breathing. The measurement setup for performing an experiment on an 3D model includes a sensor system with pressure sensors and a data acquisition system. The pressure sensing was developed based on piezoresistive pressure sensors. The piezoresistive pressure sensors were connected by thin shunt tubes with multiple places within the solid model for the pressure drop fixing of air flow in time. Installation of shunt tubes in the right places of the solid-state model was performed at the medical clinic Modern Medical Technologies with the help of an endoscope. The measuring system and locations of the shunt tubes to the pressure sensors are shown in Fig. 1. Method of measurements is based on the measurement of pressure in the paths of air flow motion in the 3D model and on data processing.

Results – The data obtained during the experiment was recorded in a data file. Further processing of the data in the Matlab mathematical modelling package allowed us to obtain 10 graphs of pressure dependence on time (Fig. 2) and 10 graphs of its power spectral density (Fig. 3) for the left part of the solid model of the nasal cavity. A similar result was obtained for the right half of the nose model. Also, by constructing the mutual power spectral

density and calculating the phase shift between the signals received from sensors installed in the same sagittal section, the velocities in the sections of the right and left sides of the solid-state model were calculated.
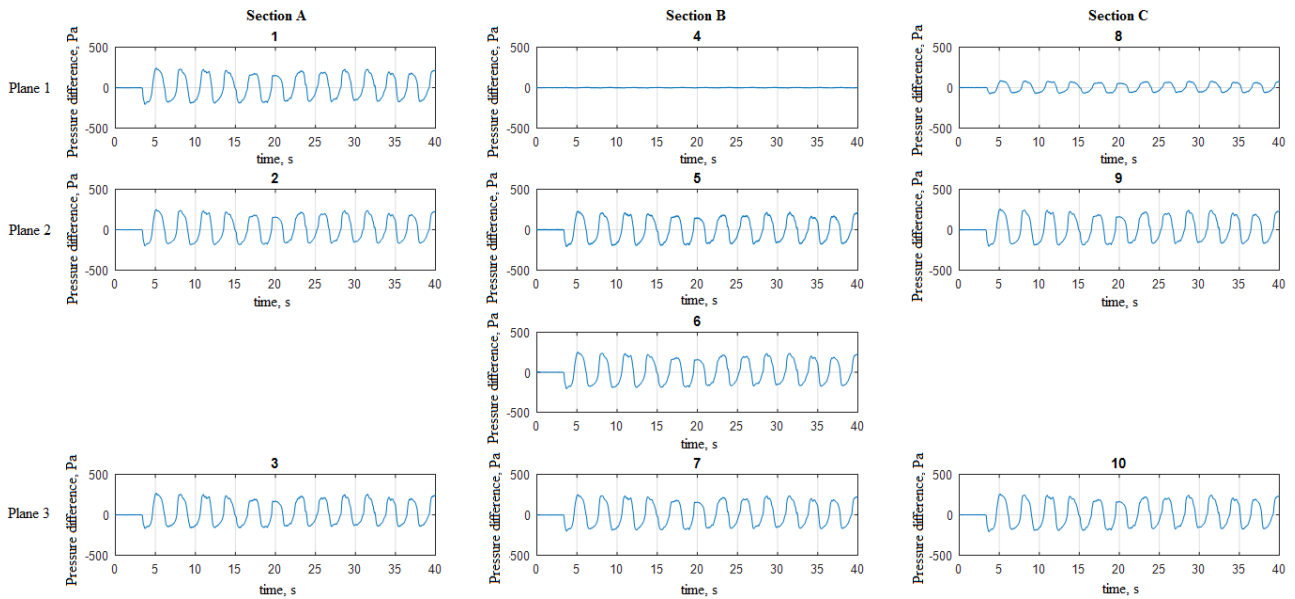

Fig.2: Results of the pressure difference measurement (1-10 are sensors numbers, planes and sections are theirs locations inside the model)
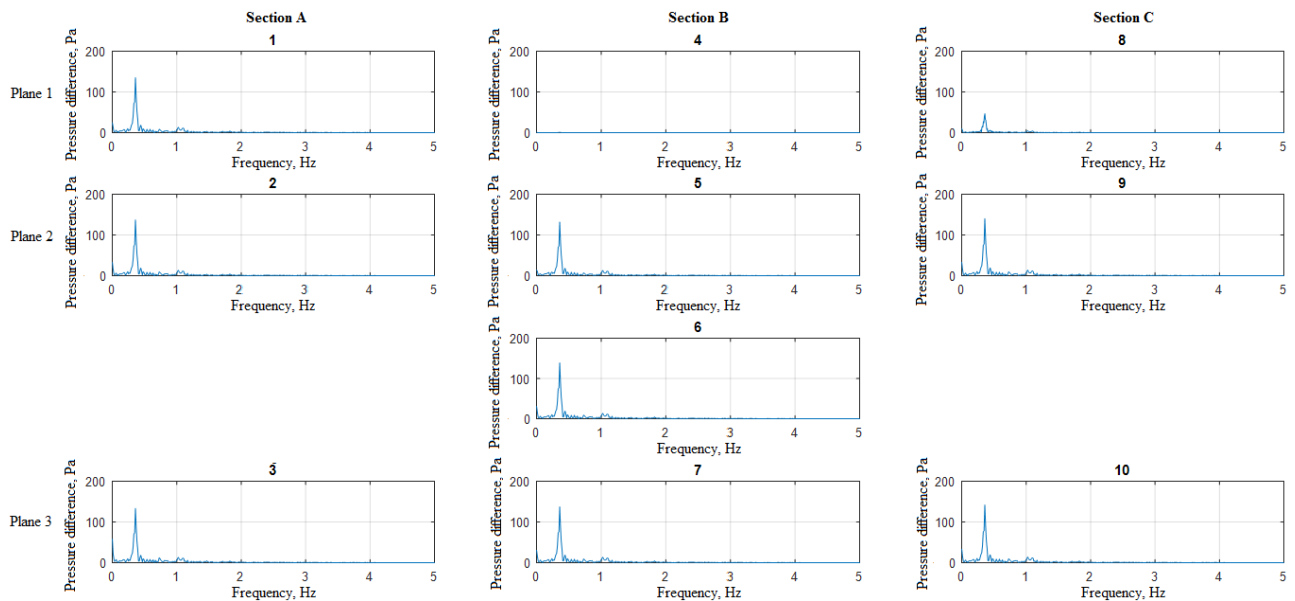
Fig.2: Power Spectral Density of measurement results (1-10 are sensors numbers, planes and sections are theirs locations inside the model)

Conclusion – Analysis of the results shows that the air, during inhaling and exhaling, moves along the bottom and middle parts of the nasal cavity. More research on this topic is presented in [3].

References

[1] G. Mlynski, S. Grutzenmacher, S. Plontke, B. Mlynski, and C. Lang, "Correlation of nasal morphology and respiratory function", J. Rhinology, 2001, 39, 197-201.

[2] G. Mlynski, S. Grutzenmacher, S. Plontke, W. Grutzmacher, B. Mlynski, P, C. Lang "A method for studying nasal air flow by means of fluid dynamics experiments", J. z. Med. Phy., 2000, 10, 207-214.

[3] G. Lukyanov, A. Rassadina, R. Neronov "Estimation of the air flow behavior in the 3D solid and numerical models of", Proceedings of the 24th Conference of Open Innovations Association FRUCT - 2019, pp. 235-242

21

Electrically conductive fibre-based sensors for smart textiles

J. Kallweit[(1)], M. Orth[(1)], A. Müller[(2)], A. Mohr[(2)], A. Minner[(3)], C. Gröber[(3)], C. Pribbernow[(3)], A. Röpert [(3)], T. Gries[(1)]

(1) Rheinisch Westfälische Technische Hochschule, Institut für Textiltechnik, Otto-Blumenthalstraße 1, 52074 Aachen, Germany
(2) Amohr Technische Textilien GmbH, Hünefeldstr. 57a, 42285 Wuppertal
(3) Interactive Wear AG, Petersbrunner Str. 3, 82319 Starnberg
E-Mail: jan.kallweit@ita.rwth-aachen.de; Web: www.ita.rwth.aachen.de;

Abstract

Textile fibres containing carbon nanotubes (CNTs) have gained great interest due to their high mechanical, electrical, magnetic and thermal properties recently [1]. Their property profile depends on nanocomposite properties, dispersion and orientation aspects, interfacial adhesion and polymer properties which can widely vary [2]. Using electrically conductive carbon nanomaterial such as carbon black (CB), carbon nanotubes (CNT) and graphite nanoplatelets (GNP) in polymers composites is a great way of making fibres for textile use electrically conductive without a compromise on their comfort and flexibility. When combining electrical conductivity and textile feel, these fibers can be used as sensors for smart textiles.

Even though there are a variety of methods to produce electrically conductive nanocomposite polymer fibres, bicomponent melt spinning process should be emphasized due to low price and large scale production [3], which is the subject of this work. Applying bicomponent technology with a home-made filter innovation of ITA at RWTH Aachen University may provide the possibility to produce fibres from conductive polymer composites (CPCs) with a high filler concentration [4].

Materials

The polymer matrix used was polyamide 6 (PA6), which is a typical semi-crystalline thermoplastic polymer with a wide range of engineering applications, and carbon-based nanofillers used were MWCNT und CB. The properties of used nanofiller can be seen in Table 2.

Table 1. The properties of the nanofiller

Properties	MWCNT NC7000	CB Vulcan XC72
Morphology	little rod	pellet
Carbon purity	>90%	-
Diameter	9.5 nm	<0,044 nm
Length	1.5 μm	<0,044 nm
Surface area	250–300 m2/g	254 m2/g
Bulk density	0,06 kg/cm3	0,264 kg/m3
Volume resistivity	0,001 Ohm.cm	6 Ohm.cm

Methods

CNT and CB-modified PA6 nanocomposite fibres were prepared from granular masterbatches containing 5 wt% CNT and 5 wt% CB in PA6. The masterbatches were fabricated in two levels by Nanocyl S.A (Sambreville, Belgium).

For the preparation of the PA6, 5 wt% MWCN + 5 wt% CB compound and pure PA6 granules both dried overnight at 85 °C in a vacuum oven. A pilot-scale bicomponent melt-spinning line was used for fibre production (Fourné Maschinenbau GmbH, Alfter-Impekoven, Germany). A polymer mass throughput of up to 2.5 kg/h is possible using this system. Extruder 1 (core extruder) and Extruder 2 (cladding extruder) are held at 270 ºC in the final zone. Both metering pumps (core and cladding metering pumps) are held at 270 ºC. The melt volume flow rate from the metering pump 1 (core) is varied between 3 and 12 g/min.

Analysis

The conductivity of the melt-spun filaments was determined by two-point DC resistance measurements and the fibres were visualized by optical microscopy.

The electrical resistance R_Ω was measured on single filaments with a length of about 100 mm using a DT-61 digital multimeter manufactured by MASTECH (Multimeter Warehouse, Walnut, CA, USA). The filaments are fixed between the two fasteners and contacted with two alligator clamps and bound to the multimeter. Optical microscopy was carried out to determine fibre quality using a Leica M205C (Leica Microsystems AG. Heerbrugg, Switzerland).

Results and discussion

Table 2 shows the average conductivity values for PA6/MWCNT-CB (each 5 wt%) nanocomposite filaments that were spun with different melt volume flow rates. Increasing the melt volume flow rate from 3 g/min to 6 g/min caused the conductivity to be quartered while increasing the melt volume rate from 6 g/min to 9 g/min and 12 g/min, respectively, shows no substantial conductivity change for PA6/MWCNT-CB filaments (Fig. 1a).

Table 2: Electrical volume conductivities of PA6 - 5 wt% MWCNT + 5 wt% CB nanocomposite filaments

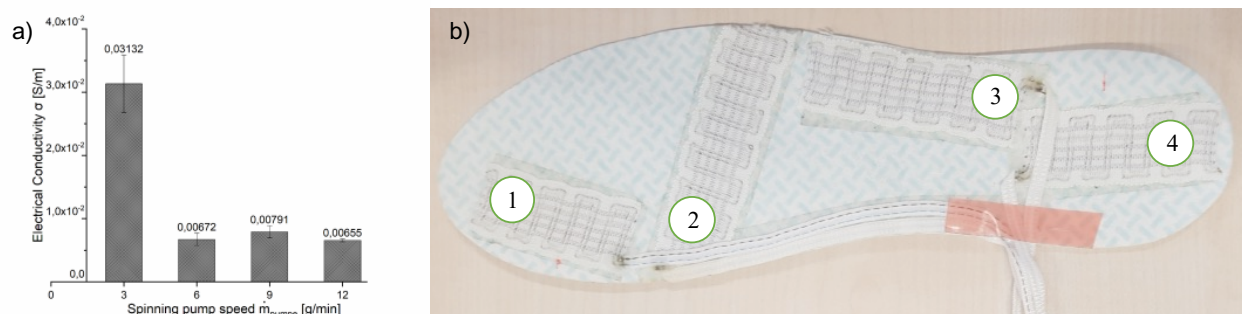| Sample	Melt volume flow rate (g/min)	Fibre diameter (µm)	Electrical Conductivity (S/m)
V1	3	336.7	3.13E-02
V2	6	486.7	6.72E-03
V3	9	490.0	7.91E-03
V4	12	506.7	6.55E-03

Fig. 1: a) The effect of melt volume flow rate on the electrical conductivity of PA6/MWCNT-CB nanocomposite fibres, b) Sensing example for a pressure sensor fiber for smart textiles.

This signifies that there is a change in sample morphology during fibre drawing, which will affect the resistivity. When the fibre morphology is changed, the percolated network structure will change, which then further affects the conductivity. The measured conductivities are at the limit of the measuring accuracy of the instrument. However, the observed effects could be reproduced in further spinning experiments and measurements. Such fibers can be used in pressure sensors, such as in the prototype in Fig. 1b, where the pressure of a foot is measured in the shoe sole at four different locations, e.g. to detect foot malpositions.

REFERENCES

[1] Yetisen, A. K.; Qu, H.; Manbachi, A.; Butt, H.; Dokmeci, M. R.; Hinestroza, J. P.; Skorobogatiy, M.: Khademhosseini, A.; Yun, S. H.: Nanotechnology in Textiles. ACS Nano 2016, 10 (3), 3042–3068.

[2] Krause, B.; Barbier, C.; Levente, J.; Klaus, M.; Pötschke, P.: Screening of Different Carbon Nanotubes in Melt-Mixed Polymer Composites with Different Polymer Matrices for Their Thermoelectrical Properties. J. Compos. Sci. 2019, 3 (4), 106.

[3] Straat M., Rigdahl M., Hagström, B.: Conducting bicomponent fibers obtained by melt spinning of PA6 and polyolefins containing high amounts of carbonaceous fillers. J. Appl. Polym. Sci. 2010, 123, 936–943.

[4] Bischoff, M.; Köhler, T.; Bandelin, J.; Möhricke, J.; Jung, R.: CNTs in Fibres Multilayered Polymerfibres for Conductive and Sensoric Applications. 17th World Text. Conf. AUTEX 2017 - Shap. Futur. Text. No. 29-31 May 2017, 032001, 1–7.

Development of a wearable polymer optical fibre-based sensor for vital signs determination under dynamic movements

J. Kallweit[(1)], T. Rauff[(1)], A. Idrissi[(1)], T. Gries[(1)]

(1) Institut für Textiltechnik (ITA) at RWTH Aachen University, Faculty of Mechanical Engineering, RWTH Aachen University, D-52074 Aachen, Germany

Abstract – Wearable sensors are experiencing a rise in their demand for several applications, such as fitness tracking, remote health monitoring, and military [1]. This work presents a polymer optical fibre (POF) based sensor for measuring respiration and heart rate, which offers relevant advantages over current available wearable measurement devices. Due to its material, this POF-based sensor has immunity to electromagnetic interference, a key aspect for patients who require monitoring while undergoing MRI procedures [2]. Additionally, its low weight, as well as the brittleness, robustness and mechanical resistance of POFs make the textile integration possible at a low cost [3]. For this work, the manufacture of a POF-based smart wearable sensor is automated and reproduceable by tailored fibre placement in an embroidery machine. Furthermore, an optimization procedure is performed to obtain the best possible sensor accuracy while keeping the textile integration and possible commercialization requirements under consideration.

Working principle – The principle of the presented POF-based sensor relies on measuring the light intensity attenuation detected at one end of the fibre with a photodiode. Light is emitted with a red LED through the fibre. To obtain a power attenuation, the fibre is embedded in an elastic textile, purposely increasing the macro bending losses by creating sinusoidal curvatures (see Fig. 1). As the textile is stretched, the amount of optical power detected by the photodiode will change due to the variation of the macro bending losses. Consequently, when the textile is attached to its user´s chest or abdomen, the inhalation and exhalation will cause it to stretch, enabling the determination of the respiration rate by analyzing the changes in the detected signal values, using a microcontroller for the measurement and digitalization. Further signal processing is possible with the use of Matlab®.
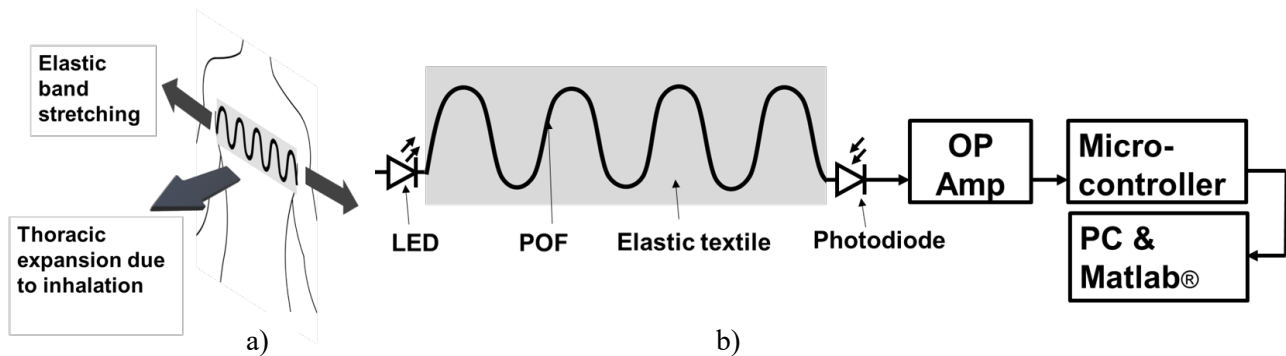

Fig.1: a) Principle of proposed sensor: Thoracic expansion during respiration causes an elongation of the textile, causing an intensity variation that can be measured. b) Schematic setup of the data acquisition process based on [4]

Design method – This work emphasizes on finding an ideal trade-off between sensor size and sensor sensitivity, as optimizing its component´s dimensions for improved textile integration and aesthetics might harm sensor accuracy and sensitivity. Several parameters must be considered that influence both sensor sensitivity and size, most importantly the fibre´s diameter, number of bends (sensitivity zones), amplitude of the sinusoidal fibre configuration and the curvature radius.

To determine the optimal parameters, the first step is to define the maximal length of the sensor, which is restricted by the width of the user´s chest. Then, the curvature radius is varied to find the value resulting in the highest sensitivity without causing too much stress on the fibre to break. Finally, the remaining parameter that affects sensor length, namely the number of bends, can be optimized. The remaining factors, amplitude and POF diameter, do not affect the length and are tested separately, but are the key factors which influence textile integration possibilities and aesthetics. Additionally, the macro bending losses at the curvatures are dependent on the POF diameter, reason for which fibres of different diameters are tested to find a compromise between textile

integration and sensitivity.

Results – Amplitudes between 5.5 cm and 7.5 cm were tested, showing no significant difference in sensor sensitivity, but a more robust and stable manufacturing process is obtained for higher amplitudes. Regarding the number of bends N, N = 6, N = 7 and N = 9 were tested. An uneven N is preferred for a better optical coupling, as both ends of the fibre point towards the same direction. In this case, the higher N delivered the best sensitivity, even though each curvature does not experience as much elongation as in the case for N = 7. As for the curvature radius, results showed that a smaller curvature radius improves the sensitivity, while also reducing the length of the sensor. A too small curvature radius increases the fibre´s chances to break. Last, a smaller POF diameter, allows a more elegant textile integration, at the cost of a slight decrease of sensitivity.

Higher sensitivity is required for heart rate determination. To further increase sensitivity, methods to remove jacket, cladding and even a part of the core (see Fig. 2) at the sensitivity zones are available [5]. Initial tests have been performed to remove jacket and cladding and measure the intensity loss before and after the removal, with promising results. However, a method to obtain reproduceable results by standardizing the process is being explored.
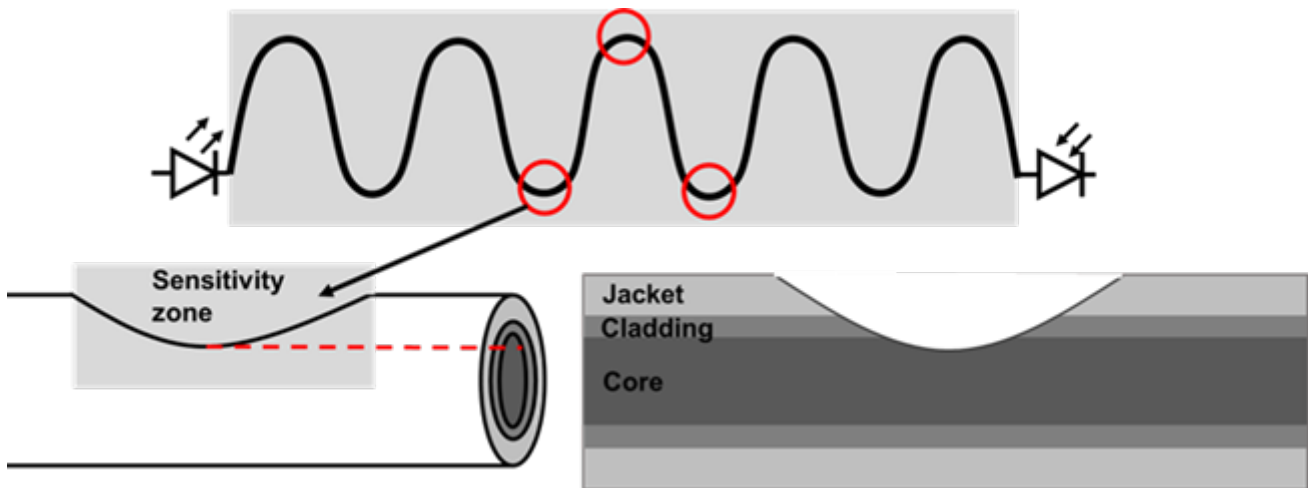

Fig.2: Fibres at the sensitivity zones, after removal of the parts.

References
[1] Wadhwani P, Gankar S (2017) Smart Clothing Market Size By Product (T-shirts, Pants, Shoes, Undergarments, Jackets, Socks), By Application (Sports & Fitness, Healthcare, Military & Defense, Industrial, Entertainment), Industry Analysis Report, Regional Outlook, Growth Potential, Price Trends, Competitive Market Share & Forecast, 2017 – 2024

[2] Dziuda L, Lewandowski J, Skibniewski F et al. (2012) Fibre-optic Sensor for Respiration and Heart Rate Monitoring in the MRI Environment. Procedia Engineering 47: 1291–1294. doi: 10.1016/j.proeng.2012.09.391

[3] Krehel M, Schmid M, Rossi RM et al. (2014) An optical fibre-based sensor for respiratory monitoring. Sensors (Basel) 14(7): 13088–13101. doi: 10.3390/s140713088

[4] Leal-Junior AG, Díaz CR, Leitão C et al. (2019) Polymer optical fiber-based sensor for simultaneous measurement of breath and heart rate under dynamic movements. Optics & Laser Technology 109: 429–436. doi: 10.1016/j.optlastec.2018.08.036

[5] Bilro L, Alberto N, Sa LM et al. (2011) Analytical Analysis of Side-Polished Plastic Optical Fiber as Curvature and Refractive Index Sensor. J. Lightwave Technol. 29(6): 864–870. doi: 10.1109/JLT.2011.2105462

Orbital Angular Momentum Mode Order Conversion with Helically Arranged Spherical Dielectric Resonator Arrays

M. Haj Hassan[(1)], B. Sievert[(1)], A. Mostafa Ahmad[(2)], A. Alhaj Abbas[(3)], A. Rennings[(1)],
K. Solbach[(3)], T. Kaiser[(3)], A. Sezgin[(2)], and D. Erni[(1)]

(1) General and Theoretical Electrical Engineering (ATE), Faculty of Engineering, University of Duisburg-Essen, and
CENIDE – Center for Nanointegration Duisburg-Essen, D-47048 Duisburg, Germany,
(2) Institute of Digital Communication Systems, Ruhr University Bochum, D-44801 Bochum, Germany,
(3) Institute of Digital Signal Processing, University of Duisburg-Essen, D-47048 Duisburg, Germany,
E-Mail: mohamed.haj-hassan@uni-due.de; Web: http://www.ate.uni-due.de;

Vortex waves – Electromagnetic (EM) waves can carry spin angular momentum (SAM) when circularly polarized and orbital angular momentum (OAM) in the form of a vortex wave. The spin angular momentum, which is today well known in circularly polarized plane waves respective gaussian beams, has already been extensively studied and researched by many engineers in contrast to the OAM in vortex waves, which is a rather new topic in the area of RF engineering. OAM waves have an unlimited number of states m (i.e. the OAM mode order), which may define a new degree of freedom that allows to transmit multiple signals at the same frequency and at the same time and thus bears the potential for novel MIMO communication schemes.

Vortex wave excitation – There are many approaches to generate vortex waves like spiral phase plates (SPP) [1], holographic plates (HP) [2], metsaurfaces [3], (dual mode) elliptical patch antennas [4], and uniform circular patch antenna arrays [5]. The vortex waves are characterized by a doughnut-shaped radiation pattern with an associated helical phase distribution that changes linearly along the beam axis, having a phase singularity in the beam center where the phase is not defined but hidden by the zero in the radiation pattern. A new approach for vortex beam generation relies a structured resonant target [6] that consists of a helical arrangement of spherical dielectric resonators (DRs), which can interact with an impinging electromagnetic wave yielding vortex beams in reflection [7] and in transmission (each of which with a corresponding OAM mode order).

Illumination setup with helically structured target – The setup consists of a circular array of planar patch antennas, which is complemented by a particularly tailored lens [8] and directed towards a structured target consisting of helical arrangement of spherical DRs. The scattered signal from a DR depends on the size, on the relative permittivity ε_r, on the loss tangent (tanδ) and on the position of the DR. In case of a spherical DR, three groups of mode are supported (*TE*, *TM* and *HE*) when illuminated by an external plane wave.

Here in this paper, a rectangular patch antenna element is designed using the EM field simulator (FEKO), that is based on the Method of Moments (MoM). Without loss of generality the operating frequency is set to 10 GHz in order to ease subsequent experimental studies. The patch antenna is matched to 50 Ω. Moreover, the patch antenna is periodically arranged to form a circular patch array of 8 antenna elements aiming at the generation of a beam with e.g. OAM mode order $m = +1$. The distance between the adjacent antenna elements is $\lambda/2$ in order to reduce the side lobe level (SLL) and to increase the gain. Unfortunately, vortex beams are suffering from a considerable beam divergence, which can be counteracted with a correspondingly tailored lens [8]. The structured target is setup as a helically arrangement of 8 spherical DRs forming a helical array. This target displays 8 resonant scatterers that are individually excited with a corresponding "delay" given by the relative position of the DR with respect to the phase of an impinging wave from the circular patch array. Adjusting the height h between adjacent DRs (i.e. the separation distance along the helical axis), yields a phase delay for each DR element that may conform to the phase relations within a propagating vortex beam enabling OAM mode conversion due to OAM conservation. The DR with radius of 2.43 mm and a relative permittivity of 37 (ceramic), the spherical DR supports a HE_{11} mode at 10 GHz. The helically structured target is therefore apt to convert impinging vortex beams into reflected and transmitted beams with converted OAM mode orders as illustrated in Fig. 1.

OAM mode order conversion – Vortex beams with different OAM mode orders [namely 0 (a), +1 (b), –1 (c), +2 (d), and –2 (e), where the labels are set according to Fig. 1] are emitted from the lensed patch antenna array towards the structured target that is configured according to the OAM mode order –1. The OAM mode order emitted from the array antenna and the one inscribed into the helical target will be compensated yielding a reflected beam with converted OAM mode order and a transmitted beam that keeps the OAM mode order of the impinging beam. Hence, in the case (a) OAM mode order 0 is generated and converted to OAM mode order –1. In the case of (b) and (c) the OAM mode orders +1 and –1 are generated and converted into the OAM mode order 0 and –2, respectively. Similarly, the case (d) and (e) generate the OAM mode orders +2 and –2 and convert them into OAM mode orders +1 and –3. Please note that the phase pattern of the reflected (converted) beam for exciting mode order –2 is slightly distorted. This is due to the strong divergence of the doughnut-shaped OAM beams with mode orders ±2, which will lead to an increasing mask out of the helical

target. Please note that the incident beam from the antenna and the transmitted beam have the same OAM mode order. In Fig. 1 we therefore display only the forward (transmitted) and backward (reflected) scattered beam, for visualization purposes as the incident beam is considerably stronger than the two scattered beams.

Conclusion – We have shown that the OAM mode orders of both, the incident (transmitted) and reflected vortex beam together with the OAM mode order of a helical target are interlinked by a simple «algebra» due to OAM conservation. This opens the field for novel target sensing/location schemes with inherent clutter suppression and enables even more complex applications such as e.g. chipless OAM-coded RFID tags [7].
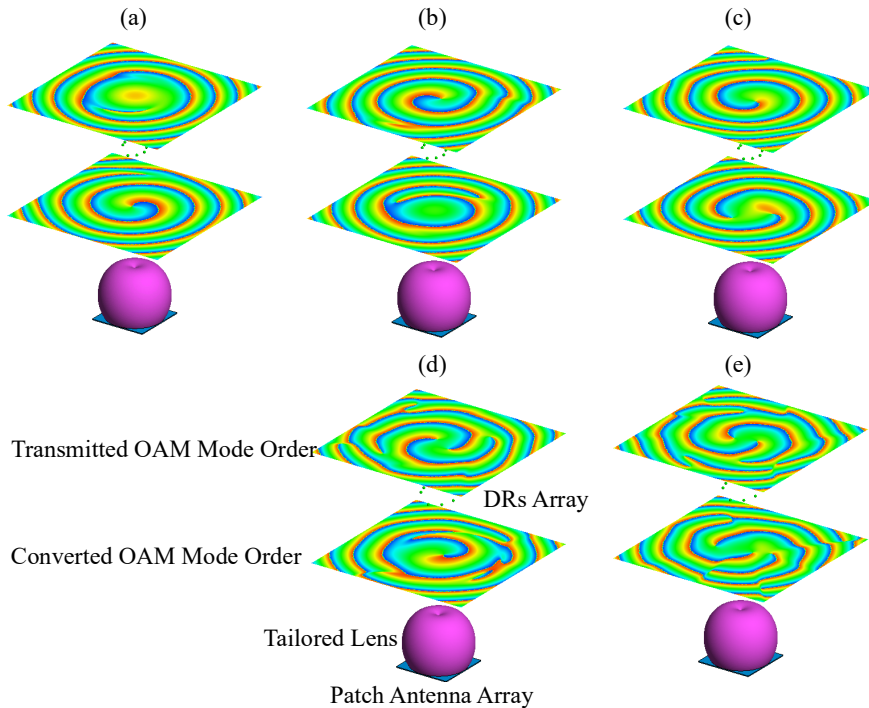

Fig.1: Different simulated scenarios for OAM mode conversion from the incident/transmitted OAM mode order to the reflected OAM mode order showing the phase distribution of the reflected and transmitted beams only: (a) 0 to –1; (b) +1 to 0; (c) –1 to –2; (d) +2 to +1; and (e) –2 to –3 (distorted). The helical target is configured according to the OAM mode order –1.

References

[1] H. M Liu, K. Yan, S. Wu, C. Li, C. Chang, and G. Fang, "Study on the terahertz vortex imaging based on spiral phase plates," 44th Int. Conf. on Infrared, Millimeter, and Terahertz Waves (IRMMW-THz 2019), Sept. 1-6, Paris, France, 2019.

[2] F. E. Mahmouli and S. Walker, "Orbital angular momentum generation in a 60 GHz wireless radio channel," 20th Telecommun. Forum (TELFOR 2012), Nov. 20-22, Belgrade, Serbia, pp. 315-318, 2012.

[3] Z. Chang, L.-S. Wu, M. Tang, Y.-P. Zhang, and J.-F. Mao, "Generation of thz wave with orbital angular momentum by graphene patch reflectarray," 2015 Int. Microw. Workshop Series on Adv. Materials and Processes for RF and THz Appl. (IMWS-AMP 2015), July 1-3, Suzhou, China, 2015.

[4] J. J. Chen, Q. N. Lu, F. F. Dong, J. J. Yang, and M. Huang, "Wireless OAM transmission system based on elliptical microstrip patch antenna, " Opt. Express, vol. 24, no. 11, pp. 11531–11538, May 30, 2016.

[5] M. Haj Hassan, M. Al-Mulla, B. Sievert, A. Rennings, and D. Erni, "Evaluation of different phased array approaches for orbital angular momentum beam steering," 13th German Microwave Conference (GeMiC 2020), March 9-11, Cottbus, Germany, pp. 44-47, 2020.

[6] A. A. Abbas, M. El-Absi, A. Abuelhaijay, K. Solbach, and T. Kaiser, "THz passive RFID tag based on dielectric resonator linear array," 2nd Int. Workshop on Mobile THz Systems (IWMTS 2019), July 1-3, Bad Neuenahr, Germany, 2019.

[7] M. Haj Hassan, A. Alhaj Abbas, A. Jiménez Saéz, A. Mostafa Ahmed, B. Sievert, M. Schuessler, A. Rennings, K. Solbach, T. Kaiser, R. Jakoby, A. Sezgin, and D. Erni, "Passive orbital angular momentum RFID tag based on dielectric resonator arrays," submitted to 3rd Int. Workshop on Mobile THz Systems (IWMTS 2020), July 2-3, Essen, Germany, 2020.

[8] M. Haj Hassan, B. Sievert, A. Rennings, and D. Erni, "Reducing the divergence of vortex waves with a lens tailored to the utilized circular antenna array," 2nd Int. Workshop on Mobile THz Systems (IWMTS 2019), July 1-3, Bad Neuenahr, Germany, 2019.

Limits of homogenization in electromagnetic composite material models: A show case in tissue analysis

K. Jerbic[(1)], B. Sievert[(1)], J. T. Svejda[(1)], J. Jebramcik[(2)], J. Barowski[(2)], A. Rennings[(1)], I. Rolfes[(2)], and D. Erni[(1)]

(1) General and Theoretical Electrical Engineering (ATE), Faculty of Engineering, University of Duisburg-Essen, and
CENIDE – Center for Nanointegration Duisburg-Essen, D-47048 Duisburg, Germany,
(2) Institute of Microwave Systems, Ruhr University Bochum, D-44801 Bochum, Germany,
E-Mail: kevin.jerbic@uni-due.de; Web: http://www.ate.uni-due.de;

EM characterization of material composites – The proper knowledge of the electromagnetic (EM) properties of composites has become an integral part for the development of measurement equipment and techniques in industrial and medical applications. Due to its potential to resolve both material and structural/morphological features, mobile integrated electronic systems operating at lower THz frequencies has currently gained a great deal of interest [1]. Because of its simple applicability, the development of contactless, noninvasive material characterization/classification schemes turned out to be an appealing vision and has been successfully employed for e.g. the detection and assessment of delamination in glass fiber-reinforced composites by detecting their structural characteristics [2], [3], and to distinguish transgenic from non-transgenic rice seeds by using its spectral finger print [4] in the range of 60 GHz up to 4 THz. Another field of application for THz technology is medical imaging and diagnostics [5]. In this context, the assessment of e.g. burn injuries and the discrimination of healthy and cancerous tissue have proven to be particularly promising for investigations in reflection mode [6], [7].

Multi-scale modeling – In these reflectometry scenarios, computational EM multi-scale models are becoming increasingly important to maximize sensitivity and selectivity with respect to material textures and properties, which may be supported by machine learning and regression analysis approaches. The great difficulty in developing such tissue models, however, is the highly complex multiscale morphology of the biological tissue, which determines the macroscopic EM properties. The development of such virtual tissue models can therefore be regarded as one of the most meaningful benchmark problems with respect to the EM simulation of composite material systems.

Based on this premise, we developed a numerical three-stage methodology, which is implemented in the framework of a *multi-scale EM simulation workbench* to explore a generic hypodermis (HYP) tissue. First, the presented procedure is based on a hierarchically organized multiscale approach that starts on the skin's proper cellular length scale, and evolves step-by-step through the structural length scales of the tissue's morphology while using a numerical homogenization procedure that provides both the dispersive and tensorial EM material properties of the corresponding tissue composite [8]. Second, after this bottom-up homogenization, both tissue models, namely the heterogenous reference model and its effective material theory (EMT) representation are evaluated and compared in a numerical reflectometry setup shown in Fig. 1. And third, the validity limits of the HYP's homogenized material representation based on the EMT are explored within a subsequent Monte-Carlo analysis [9], which examines 1980 implementations of fictitious HYP derivatives with different volume fractions of the cellular and extracellular material $c_v \in \{0.05; 0.10; \dots ; 0.45\}$.
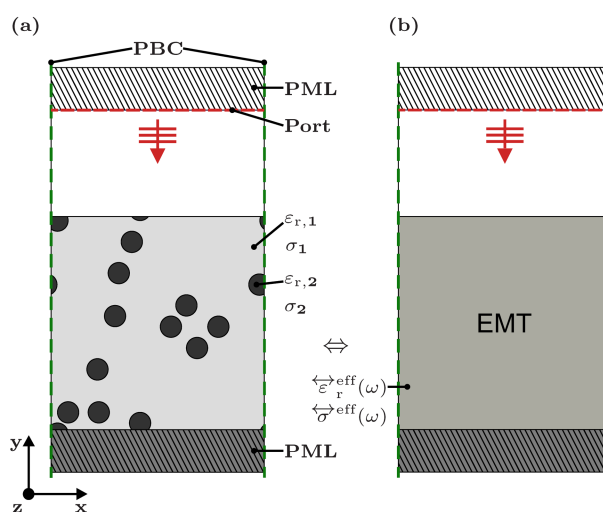

Fig. 1: Schematic of the simulated mm-wave/THz reflectometry setup that has been implemented in COMSOL Multiphysics: (a) the heterogeneous material structure; (b) the equivalent homogeneous representation based on the effective material theory (EMT).

Validity limits – The results of the Monte-Carlo analysis (cf. Fig. 2) revealed validity limits for HYP tissues at astonishingly low frequencies around 60-80 GHz above which the EMT representation breaks down. In the following great significance has been attributed to the documentation of this «collapse» since it may impact

future schemes of e.g. virtual histopathology in the mm-wave/THz range.

Currently we are working on the validation of our EM multi-scale modeling approach using various 3D printed artificial composites with different fillings. Some composites are undergoing corresponding frequency scaling in order address the interesting ranges in the frequency response of the power reflection as the latter has to be confined to the given operating bandwidth of the measurement setup.
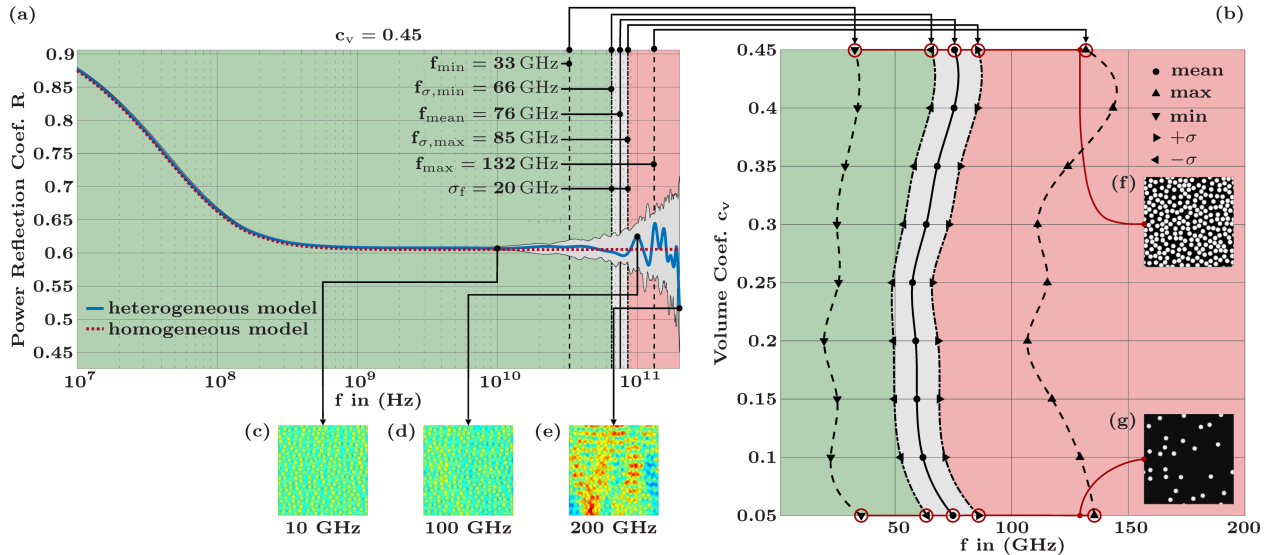

Fig. 2: Validity limits for several generic HYP derivatives:(a) spectral responses of the reflectance (showing the typical Maxwell-Wagner roll-off in the MHz range) of 1980 implementations for εr,1 = 80; σ1 = 0.53 S/m; εr,2 = 50; σ1 = 0.12 S/m; dinc = 50 μm, and volume fraction cv = 0.45; (b) Validity limits of the derivatives of a heterogeneous material structure (here the HYP tissue); (c), (d), (e) examples of the electric field distribution IEI at various frequencies (i.e. at 10 GHz, 100 GHz, 200 GHz, respectively); (f), (g) examples of the analyzed microstructures (i.e. for cv = 0.45 and cv = 0.05 respectively). The validity range of the EMT material model is colored in «green» while the forbidden range is marked «red».

References

[1]   P. Hillger, M. van Delden, U. S. M. Thanthrige, A. M. I. Ahmed, J.Wittemeier, K. Arzi, B. S. M. Andre, W. Prost, A. Rennings, D. Erni, T. Musch, N. Weimann, A. Sezgin, N. Pohl, and U. R. Pfeiffer, "Toward mobile integrated electronic systems at THz frequencies," submitted to J. Infrared Millim. Terahertz Waves, 2020.

[2]   J. Dong, B. Kim, A. Locquet, P. McKeon, N. Declercq, and D. S. Citrin, "Nondestructive evaluation of forced delamination in glass fiber reinforced composites by terahertz and ultrasonic waves," Compos. Part B: Eng., vol. 79, pp. 667–675, 2015.

[3]   J. Dong, A. Locquet, N. F. Declercq, and D. S. Citrin, "Polarizationresolved terahertz imaging of intra- and inter-laminar damages in hybrid fiber-reinforced composite laminate subject to low-velocity impact," Compos. Part B: Eng., vol. 92, pp. 167–174, 2016.

[4]   X. Hu, W. Lang, W. Liu, X. Xu, J. Yang, and L. Zheng, "A nondestructive terahertz spectroscopy-based method for transgenic rice seed discrimination via sparse representation," J. Infrared Millim. Terahertz Waves, vol. 38, no. 8, pp. 980–991, 2017.

[5]   F. Toepfer and J. Oberhammer, "Millimeter-wave tissue diagnosis: The most promising fields for medical applications, " IEEE Microw. Mag., vol. 16, no. 4, pp. 97–113, 2015.

[6]   D. Oppelt, J. Adametz, J. Groh, O. Goertz, and M. Vossiek, "MIMO-SAR based millimeter-wave imaging for contactless assessment of burned skin," 2017 IEEE MTT-S International Microwave Symposium (IMS 2017), June 4-9, Honolulu, HI, USA, pp. 1383-1386, 2017.

[7]   K. I. Zaytsev, I. N. Dolganova, N. V. Chernomyrdin, G. M. Katyba, A. A. Gavdush, O. P. Cherkasova, G. Komandin, M. A. Shchedrina, A. N. Khodan, D. S. Ponomarev, I. V. Reshetov, V. Karasik, M. Skorobogatiy, V. N. Kurlov, and V. V. Tuchin, "The progress and perspectives of terahertz technology for diagnosis of neoplasms: A review," J. Opt., vol. 22, no. 1, pp. 1–44, 2019.

[8]   J. Froehlich, S. Huclova, C. Beyer, and D. Erni, book chapter 12 "Accurate multi-scale skin model suitable for determining sensitivity and specificity of changes of skin components," pp. 353-394, in Computational Biophysics of the Skin, Bernard Querleux (Ed.), Singapore: Pan Stanford Publishing Pte. Ltd., (ISBN-978-981-4463-84-3), 2014.

[9]   K. Jerbic, B. Sievert, J. T. Svejda, A. Rennings, and D. Erni, "On the applicability of homogenization in composite material models for tissue analysis in the mm-wave range," Photonics & Electromagnetics Research Symposium/Progress in Electromagnetics Research Symposium (PIERS 2019), June 17-20, University of Rome 'La Sapienza', Rome, Italy, Session 3P3 – SC1 & SC2: 'Computational Bioelectromagnetics: from Single Molecule to Human Body', pp. 1717-1718, 2019.

Fitting X-Markers with modified Aruco-Tags for unique detection in Multi-Stereo-Camera Systems

O. Gieseler[1], H. Roth[1,2], J. Wahrburg[1,2]

(1) Center for Sensorsystems (ZESS) at University of Siegen, Faculty of Engineering, D-57076 Siegen, Germany
(2) Institute of Control Engineering at University of Siegen, D-57076 Siegen, Germany
E-Mail: gieseler@zess.uni-siegen.de; Web: www.zess.uni-siegen.de/modicas

Abstract – We found a new approach to improve detection of X-Markers in multi-stereo camera navigation. We add Aruco markers to the X-Marker shape to make them unique and distinguishable. For this we propose three stages of combinations. Coding Reference Bodies with Arucos, coding X-Markers with two Arucos and Coding X-Markers with four Arucos. The position of the X-Markers shall be found out from the marker center. A region of interest is defined by means of the Arucos to decrease the search area for the corner detector. Additionally, Aruco marker information (corners) can help to evaluate and refine the X-Marker center position. Also, Aruco marker shall ease the correlation of X-Markers in all camera image and replace epipolar or fundamental matrix calculations. Overall we expect a decreased computation time for corner detector and marker correlation algorithms.

Introduction – Using artificial landmarks is common to locate the pose of instruments and patients in navigated and robot assisted surgery. Mostly, retroreflective sphere markers or X-Markers combined to a reference body are applied. It is possible to locate them in millimetre or submillimetre range with properly calibrated stereo cameras [1],[2]. Using more than two cameras in a multi-stereo system a disadvantage arises: The markers are not unique and therefore not distinguishable. Thus, before the calculation of their 3D position the markers have to be correlated in the single pictures of each camera. For this, computation time is rising with the number of cameras and the number of markers per picture. Therefore we tried to find a distinguishing feature which can be added to the markers to make them unique and thus facilitate direct correlation. We choose Aruco markers as additional features. An Aruco is a quadratic marker with a black frame and 16 (4x4) small black and white squares pattern inside (see Fig. 1).
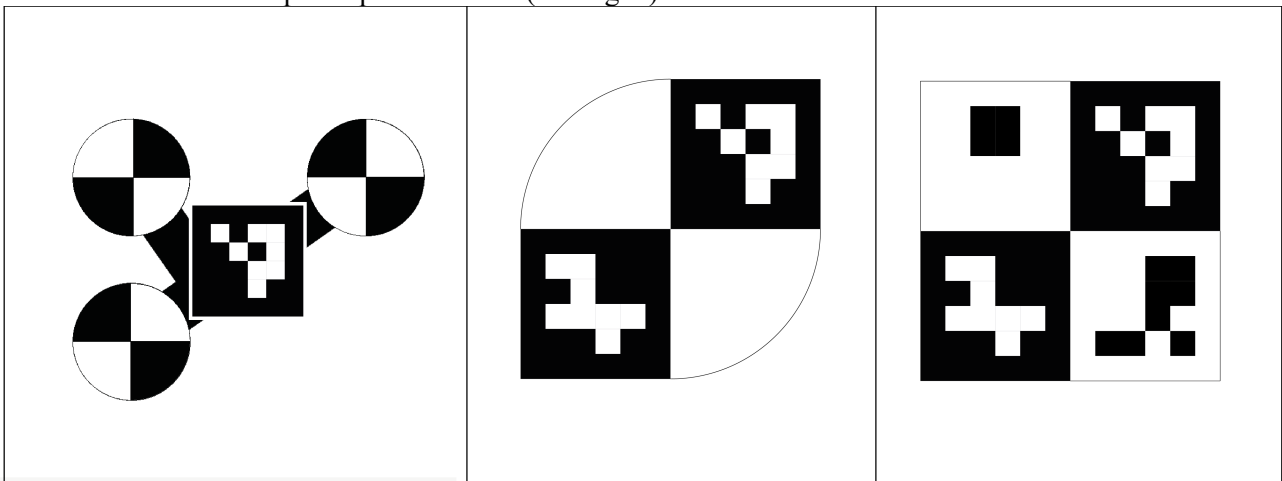

Fig.1: (a) Reference body with Aruco, (b) X-Marker coded with two Arucos, (c) X-Marker coded with four Arucos

Materials and Methods – We use X-Markers for multi-stereo camera navigation and add Aruco markers to the shape to make them unique. While the Aruco markers are used for distinctness, X-Markers are used for position determination. We employ the 4x4 Aruco markers and detection algorithm created by Garrido-Jurado et al. [3]. It is available as open source code in emguCV and uses a predefined dataset of markers called dictionary which contains the Aruco marker template shapes. The algorithm detects Arucos and provides the marker ID and the pixel coordinates of all four corners. Additionally, it assigns a coordinate system to the Aruco, so that the orientation in the camera picture is also given. This brings us to the following three stages of X-Marker coding with Arucos. First we try to code a reference body (RB) containing three X-Markers with an Aruco, correlating the X-markers by their position relative to the Aruco (vicinity to the different corners) (Fig. 1a). Secondly, we fused both marker types, placing two Arucos in the black sectors of an X-Marker. Choosing those markers from a dictionary which have a large black area. Together with the black frame those Arucos contain black squares of 3 by 3 fields pointing to the corner of the X-Marker (Fig. 1b). The third stage

is to place Arucos additionally in the white sectors of the X-Marker in the same way like described before, but inverting them to get a white frame and largest possible white areas pointing to the edge, so that the X-Marker shape remains in the center area (Fig. 1c).

Applying the Aruco detection algorithm provides all Arucos in an X-Marker. This enables recognition of the X-Marker and helps us to define a region of interest between the Arucos where we apply a corner detection algorithm to find the center of the X-Marker. Further we can use the given corner coordinates of the Arucos to evaluate the result by comparing the inner corners of the Aruco and additionally calculating diagonals between the outer corners. Thereby we are able to calculate a probable X-Marker center independent from the corner detector by averaging all information from the Arucos (Fig. 2).
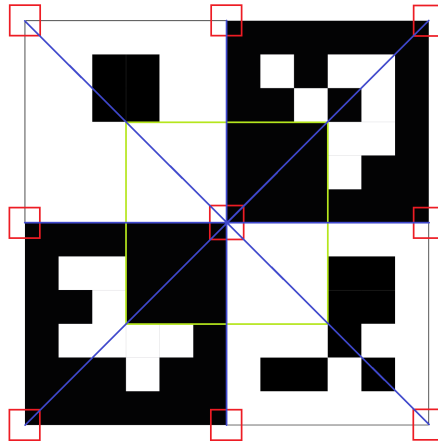

Fig.2: Aruco marker with corners provided by the Aruco detector (red), region of
interest (green) and diagonals crossing in the X-Marker center (blue)

Results and Discussion– We created X-Markers coded with different Arucos and printed them on paper with an accurate printer. The Arucos are properly recognized in the camera pictures. The corners detected by the corner detector could be reduced from some thousands found in the whole picture with background to a small two digit number in the defined region of interest. By applying the corner detector just on the regions of interest the computation time which is depending on the size of the search area could be decreased. Instead of 1920x1200 only areas of 20x20 pixels per marker have to be processed.

The correlation of the markers is done by identification of the Aruco IDs. With this knowledge it is easy to correlate each marker in all pictures. Common procedures for correlation analysis are either epipolar geometry inspection for stereo camera systems or fundamental matrix criteria for more than two cameras. Both, the operations itself for every new picture and marker and necessary pre-calculations cause a high computing effort and computation time is rising with the number of cameras and the number of markers per picture.

In average Aruco detection needs 11 ms for a 24 marker dictionary in a 640x480 pixels image [3]. Currently running tests evaluate the speed of Aruco marker detection in our application and show how much faster and how accurate the new algorithm can perform and which of the three proposals (Fig. 1) provides the best results. With the new approach a significant decrease of computation time is expected for the corner detector and for marker correlation.

References
[1]   Northern Digital NDI, Waterloo, Ontario, Canada, https://www.ndigital.com/products/, (Polaris Cameras)
[2]   Atracsys LLC, Puidoux, Switzerland, https://www.atracsys-measurement.com/, (fusionTrack Cameras)
[3]   S. Garrido-Jurado, R. Muñoz-Salinas, F. J. Madrid-Cuevas, and M. J. Marín-Jiménez. 2014. "Automatic generation and detection of highly reliable fiducial markers under occlusion". Pattern Recogn. 47, 6 (June 2014), 2280-2292. DOI=10.1016/j.patcog.2014.01.005

Sparse signal recovery with l_1 minimization

D. A. Hage[(1)], M. Heredia Conde[(1)], O. Loffeld[(1)]

(1) Center for Sensorsystems (ZESS), University of Siegen, Paul-Bonatz-Strasse 9-11, D-57076 Siegen, Germany
E-Mail: {hage, heredia, loffeld}@zess.uni-siegen.de ; Web: www.uni-siegen.de/zess/

Abstract – In many problems high-dimensional discrete signals need to be reconstructed from noisy and often undersampled data, raising the issue of solving nominally underdetermined, as well as noise-contaminated systems of equations. The theory of compressed sensing states (and proves) that such signals can uniquely be reconstructed under the assumption that the signals are sparse. In this work we complement the l_1-minimizing Kalman filter with an external thresholding. Let s be the sparsity and m the number of rows of the matrix A relating the n-dimensional vector to be determined to the m-dimensional vector of measurements. The results show that the l_1-minimizing Kalman filter with external thresholding (KF-ET) yields a faster algorithm for the reconstruction of x with $s/m < 0.5$ than the primal-dual algorithm for l_1-minimization of Chambolle & Pock (C&P). In the noiseless case the l_1-minimizing Kalman filter with external thresholding also needs less iterations than the Orthogonal Matching Pursuit (OMP).

Part one – extended linearized Kalman filter
For the reconstruction of x we assume that the underlying matrix fulfills the null space property. We propose understanding the l_1 norm as an additional measurement of the sparse state vector x and using an iterative extended linearized Kalman filter to approach an estimate x in a recursive manner [1], [2]. However, the Kalman filter does not directly estimate the full state vector x. Rather than that, x is decomposed into a particular solution and a null space complement.

$$x = x_p + x_N$$

The algorithm starts from the estimate of x and estimates in each iteration a difference vector with reduced l_1 norm while fulfilling the constraints $Ax = b$ in a weighted least squares sense.

Part two – Additionally, in each iteration of the l_1-minimizing Kalman filter the algorithm is determined by an external thresholding. Generally, thresholding algorithms iterate between a step of selecting a support element, and a second step of support pruning [3], [4].
Ω_k denotes the estimated support set, that contains the indices of $m/2$ largest entries in $x(k)$ at iteration k. Matrix A_{Ω_k} represents columns of A indexed by Ω_k. The resulting overdetermined system of equations of external thresholding is resolved via a Maximum Likelihood Estimator [5]:

$$x_{\Omega_k} = \left(A_{\Omega_k}^H R^{-1} A_{\Omega_k} \right)^{-1} A_{\Omega_k} R^{-1} b$$

Part three – In the following table we give a few examples of the performance of the l_1-minimizing Kalman filter with external thresholding (KF-ET).

m	n	s	number of iterations	$\|\hat{x} - x\|_1$	$\|\hat{x} - x\|_2$
64	128	10	2	3.9×10^{-15}	9.9×10^{-16}
120	256	20	11	5.7×10^{-15}	1.2×10^{-15}
400	1024	100	22	1.1×10^{-14}	1.7×10^{-15}
1200	4096	250	20	2.3×10^{-14}	2.1×10^{-15}
5000	8000	500	13	7.4×10^{-14}	3.0×10^{-15}
10000	15000	1000	20	1.1×10^{-13}	3.9×10^{-15}

Table: Calculation of l_1-minimizing Kalman filter with external thresholding and abort criterion $\varepsilon = 10^{-10}$.

The number of iterations, required for the reconstruction $\hat{x}$, is less than the sparsity s of the exact solution x.

The first example in the table shows that the KF-ET stopped after 2 iterations with a normalized sparse recovery error norm of 10^{-16} even though the sparsity is 10. In the last example we observe that the number of iterations is only a small percentage of the sparsity s.

For further experiments we use DTG (Donoho-Tanner graphs) [6] with $n = 256$ dimensionality. Each pixel of the graphs will show the average value of 16 individual experiments. We compare the normalized sparse recovery error and the recovery time of the KF-ET, the C&P [7] and the OMP [8],[9].

The proposed KF-ET shows both, better recovery performance and faster recovery, than the C&P and the OMP [10]. In [10] the l_1-minimzing Kalman filter with external thresholding was analyzed considering different noise variances. In almost all cases it can be observed that KF-ET – as opposed to the C&P and OMP – achieves good to excellent results. Furthermore as opposed to the OMP the KF-ET does not need to know the sparsity. Even considering noise variances, the KF-ET is stable and reliable in terms of sparse recovery error, l_0 norm of the estimates, support mismatch, and recovery time.

References

[1] O. Loffeld, A. Seel, M. Heredia Conde, L. Wang, "Sparse CS reconstruction by nullspace based l_1- minimizing Kalman filtering", 2016 International Conference on Communications (COMM), Bucharest, Romania, 9-10 June, pp. 449-454, 2016

[2] O. Loffeld, A. Seel, M. Heredia Conde, L. Wang, "A Nullspace Based l_1 Minimizing Kalman Filter Approach to Sparse CS Reconstruction", 11th European Conference on Synthetic Aperture Radar (EUSAR 2016), Germany, 6-9 June, pp. 1-5, 2016

[3] T. Blumensath, M.E. Davies, "Iterative hard thresholding for compressed sensing", Appl. Comput. Harmon. Anal., pp. 265-274, 2009

[4] T. Blumensath, M.E. Davies, "Normalised iterative hard thresholding guaranteed stability and performance", IEEE J. Sel. Topics Signal Process., vol. 4, no. 2, pp. 298-309, 2010

[5] O. Loffeld, „Estimationstheorie I: Grundlagen und stochastische Konzepte", R. Oldenbourg Verlag GmbH,München, isbn 3-486-21616-3, 1990

[6] M. Heredia Conde, "Compressive Sensing for the Photonic Mixer Device - Fundamentals, Methods and Results", Springer Vieweg, doi:10.1007/978-3-658-18057-7, 2017

[7] A. Chambolle, T. Pock, "A First-Order Primal-Dual Algorithm for Convex Problems with Applications to Imaging", J. Math. Imaging Vis. 40.1, pp. 120-145, issn: 0924-9907, 2011

[8] Y. C. Pati, R. Rezaiifar, P. S. Krishnaprasad, "Orthogonal matching pursuit: Recursive function approximation with applications to wavelet decomposition", Proc. Asilomar Conf. Signals, Syst. Comput., pp.40-44, 1993

[9] J. Tropp, A. Gilbert, "Signal recovery from random measurements via orthogonal matching pursuit", IEEE Trans. Inf. Theory, vol. 53, no. 12, pp. 4655-4666, 2007

[10] D. A. Hage, M. Heredia Conde, O. Loffeld, "New Results on Sparse Signal Recovery via Kalman-Filter-based l_1 −Minimization", IEEE Elsevier Signal Processing, doi: 10.1016/j.sigpro.2020.107487, Jan. 2020

Vibrational CARS thermometry on oxy-fuel flames established in a swirled combustion chamber

E. Sidiropoulos[(1,2)], C. Meißner[(1,2)], J. I. Hölzer[(1,2)], H. Schneider[(3)], A. Dreizler[(3)], T. Seeger[(1,2)]

(1) Institute of Engineering Thermodynamic at University of Siegen, D-57076 Siegen, Germany
(2) Center for Sensor Systems (ZESS) at University of Siegen, D-57076 Siegen, Germany
(3) Institute of Reactive Flows and Diagnostics at Technical University of Darmstadt, D-64287 Darmstadt, Germany
E-Mail: evaggelos.sidiropoulos@student.uni-siegen.de; Web: www.mb.uni-siegen.de/tts/;

Abstract – The combustion of fossil fuels releases carbon dioxide into the atmosphere, which is primarily responsible for the climate change [1-2]. In 2015, at the Climate Conference of Paris, over 190 countries decided to limit the man-made global warming to below 2 °C compared to preindustrial levels. In order to achieve this climate goal, one important measure is the reduction of carbon dioxide emissions. One promising technology is the combination of oxy-fuel combustion and carbon capture and usage/storage (CCU/CCS). The oxy-fuel process uses a mixture of recirculated exhaust gas and pure oxygen as an oxidizer instead of air. This enables the efficient use of carbon capture and storage technologies to reduce future CO_2 emissions into the atmosphere. The changes in the combustion atmosphere result in differences in the combustion behaviour. The higher molar heat capacity of CO_2 compared to N_2 leads to reduced flame temperatures. The variable oxygen content in oxy-fuel flames can be increased to achieve similar adiabatic flame temperatures. Furthermore the differences in the gas density, oxygen diffusion rate and radiation properties influence heat transfer and combustion reaction kinetics inside the combustion chamber. Additionally for solid fuels, the mechanisms of volatile release and char combustion differ. There have already been several studies on oxy-fuel combustion in combination with carbon dioxide capture and storage [3-4]. Nevertheless the detailed physical and chemical processes in oxy-fuel combustion are still not fully understood. One major state variable is the local gas temperature. Laser based measurement techniques allow non-intrusive measurements of gas temperatures with high spatial and temporal resolution.

To address these requirements an optically accessible swirled combustion chamber was used to gain a better understanding of the mechanisms of burning pulverized solid fuels in an oxy-fuel atmosphere [5].
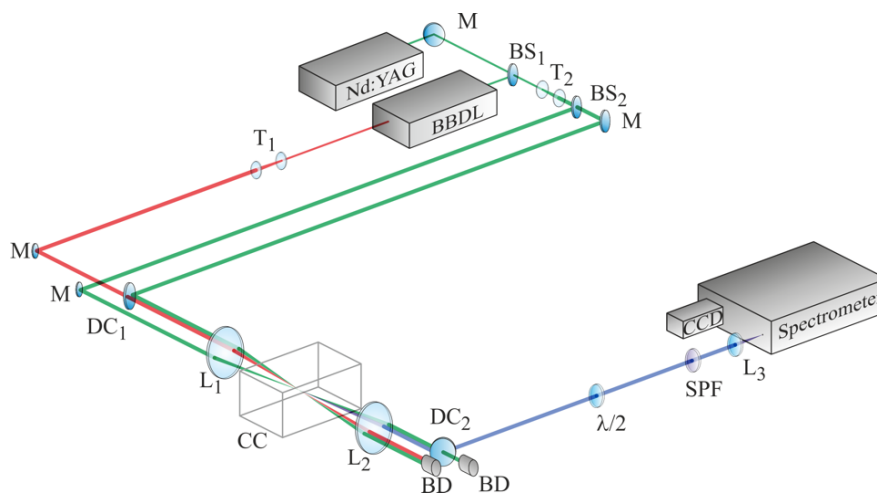

Fig. 1: Scheme of the experimental setup: BBDL, broadband dye laser; BS, beam splitter; CC, combustion chamber; M, folding mirrors; DC, dichroic mirrors; BD, beam dump; L, lenses; λ/2, half-wave plate; T, telescope; SPF, short pass filter.

A well-proven measurement technique for spatially and time resolved gas temperature determination is the coherent anti-Stokes Raman scattering technique (CARS) [6]. Due to the coherent signal character, the high signal strength and the possibility of suppressing interfering signals, CARS is particularly suitable for the use in technical combustion environments with limited optical access. The experimental vibrational CARS setup used in this work is shown in Figure 1. In air-fed combustion N_2 is usually the molecule of choice for CARS thermometry [7]. Since nitrogen molecules are almost not available in oxy-fuel combustion processes, O_2 or CO_2 has to be used as a probe molecule. Pure rotational CARS temperature measurements using O_2 as probe molecule have been performed successfully in a flame spray pyrolysis process [8-10]. Recently O_2 vibrational CARS temperature measurements have been successfully performed in an oxy-fuel combustion process in a large-scale combustion chamber for glass-melting [11], where high temperatures are required.

In this work the O_2 vibrational CARS technique was applied to an optically accessible swirl combustion chamber to gain a better understanding of the mechanisms of burning pulverized solid fuels in an oxy-fuel atmosphere. Radial temperature profiles have been recorded at different positions downstream the burner exit. Different operation conditions were investigated, in an oxy-fuel atmosphere and in air. Photographs of the investigated flames are shown in Figure 2.
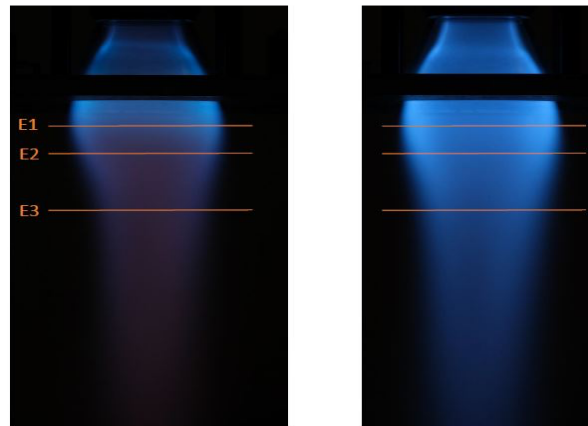

Fig. 2: Photographs of two investigated flames: Methane-air flame (left) and methane-oxy-fuel flame (right), downstream positions for CARS measurements are indicated by orange lines.

References

[1]   P. D. Jones, M. New, D. E. Parker, S. Martin and I. G. Rigor, "Surface air temperature and its changes over the past 150 years", Reviews of Geophysics, vol. 37, pp. 173-199, 1999.

[2]   J. R. Christy, R. W. Spencer and W. D. Braswell, "MSU Tropospheric Temperatures: Dataset Construction and Radiosonde Comparisons", Journal of Atmospheric and Oceanic Research, vol.17, pp.1153-1170, 2000.

[3]   R. Duckat, M. Treber, C. Bals and G. Kier, "CO2-Abscheidung und Lagerung als Beitrag zum Klimaschutz", International Workshop on Carbon Dioxide Capture and Storage 2002, November, Berlin, Germany, 2004.

[4]   R .Grünewald, "A Review of Carbon Dioxide Capture and Storage - Technology, Potentials, Risks, Costs, and Regulation", GAIA Ecological Perspectives for Science and Society, vol. 18, pp. 211-220, 2009.

[5]   L.G. Becker, H. Kosaka, B. Böhm, S. Doost, R. Knappstein, M. Habermehl, R. Kneer, J. Janicka and A. Dreizler, "Experimental investigation of flame stabilization inside the quarl of an oxyfuel swirl burner", Fuel vol. 201, pp. 124-135, 2017.

[6]   A. C. Eckbreth, "Laser diagnostics for combustion temperature and species", 2nd ed., Gordon and Breach Publishers, Amsterdam 1996.

[7]   M. C. Weikl, T. Seeger, R. Hierold and A. Leipertz, "Dual-pump CARS measurements of N2, H2 and CO in a partially premixed flame", Journal of Raman Spectroscopy, vol. 38, pp. 983-988, 2007.

[8]   S. R. Engel, A. F. Koegler, Y. Gao, D. Kilian, M. Voigt, T. Seeger, W. Peukert and A. Leipertz, "Gas phase temperature measurements in the liquid and particle regime of a flame spray pyrolysis process using O2-based pure rotational coherent anti-Stokes Raman scattering", Applied Optics, vol. 51, pp. 6063-6075, 2012.

[9]   Y. Gao, T. Seeger and A. Leipertz, "Development of temperature evaluation of pure Rotational Coherent Anti-Stokes Raman Scattering (RCARS) spectra influenced by spatial averaging effects", Proceedings of the Combustion Institute, vol. 35, pp. 3715-3722, 2015.

[10]   D. Kilian, S. Engel, B. Borsdorf, Y. Gao, A. F. Koegler, S. Kobler, T. Seeger, S. Will, A. Leipertz and W. Peukert, "Spatially resolved flame zone classification of a flame spray nanoparticle synthesis process by combining different optical techniques", Journal of Aerosol Science, vol. 69, pp. 82-97, 2014.

[11]   J. W. Tröger, C. Meißner and T. Seeger, "High temperature O2 vibrational CARS thermometry applied to a turbulent oxy-fuel combustion process", Journal of Raman Spectroscopy, vol. 47, pp. 1149-1156, 2016.

Time resolved in-cylinder combustion analysis in a reformate gas engine by using a chemiluminescence sensor system

Jürgen Wultschner[1,2], Ingo Schmitz[1,2], F. Dieding[3], D. Pennings[3], K.I. Yapici[3], S. Warkentin[4], E. Pohl[4], Thomas Seeger[1,2]

(1) Institute of Engineering Thermodynamics, University of Siegen, D-57076 Siegen, Germany
(2) Center for Sensor Systems (ZESS), University of Siegen, D-57076 Siegen, Germany
(3) ECC Automotive GmbH, D-52249 Eschweiler, Germany
(4) OWI Science for Fuels gGmbH, D-52134 Herzogenrath, Germany
E-Mail: juergen.wultschner@uni-siegen.de; Web: https://www.mb.uni-siegen.de/tts/

Abstract – The increasing global demand for energy requires, in addition to the development of renewable technologies, an optimization of conventional systems regarding their pollutant emissions and efficiency [1]. Gas powered combined heat and power plants (CHP) offer the advantage that heat is used in addition to electric energy. However, the efficiencies, especially for smaller systems below 100 kW, are not yet sufficiently high. Therefore, in this approach, the waste heat from the internal combustion engine is used to reformate the combustion gas, leading to an increased caloric value up to 15 % and an overall efficiency of more than 40%. The gas used for the reformation, essentially consisting of methane (CH_4) and carbon dioxide (CO_2), is chemically converted in hydrogen (H_2) and carbon monoxide (CO), using the exhaust heat and adding water vapor in the reformer. Consequently, in order to characterize and optimize such systems it is necessary to analyze time resolved the gas composition supplied to the engine and examine the combustion process in dependence of engine parameters.

Combustion processes are difficult to probe by conventional diagnostic techniques, since the conditions are transient, high temperatures are involved and multiple interferences, such as soot particles and background radiation may disturb measurements. Optical methods lend themselves to in-situ measurements. A major advantage of optical techniques is that they do not perturb the probed system, hence avoiding measurement errors. Nevertheless most of these methods need complicated modifications of the engines [2]. Consequently, the measurement results achieved in such modified engines are not directly transferable to serial engines. Therefore, in this work, the mixture formation and the combustion process are examined with the help of an emission spectroscopic probe, which detects the emitted light of the in-cylinder combustion process time-resolved. The optical probe adapted to the research engine has an observation window of only 2.8 mm in diameter. This ensures that the heat transfer properties of the research engine remain almost unchanged. Since the compression ratio was not changed, the results achieved here can be transferred directly to the serial engine. Figure 1a shows the setup of the applied emission spectroscopy based sensor system (ESS). The designed probe head detects light in a cone with an angle of 25°, as schematically shown in Figure 1b. The optical probe is connected to the spectrometer via a fiber. This allows spectrally and time resolved measurements of the internal combustion process. In addition, the gas composition at the exit of the reformer is analyzed with a Raman sensor simultaneously. With this sensor it is possible to perform a time-resolved determination of all major components with high accuracy [3].
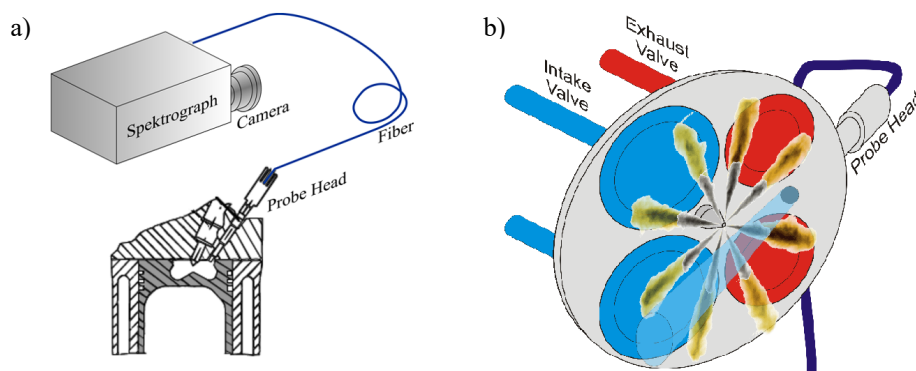

Fig.1: (a) Scheme of the ESS system setup. (b) Cylinder head equipped with the probe head.

The chemical reactions during the combustion lead to an emission of electromagnetic radiation in the ultraviolet and visible range. This radiation was used to investigate, which engine operation points ensure the most stable conditions combined with a maximum efficiency. For this investigation the hydrogen content in the combustion gas, the combustion fuel/air ratio and the exhaust gas recirculation (EGR) rate have been varied. Different exposure times with a resolution of 33 ° crank angle (CA) and 5 °CA have been selected in order to analyze either integral the complete combustion process or to use time resolved information. In each case the start of each measurement was adapted to the ignition point.

Figure 2 shows an example of an emission spectrum determined by the ESS system, with a hydrogen amount of 50.85 % and a fuel/air ratio of $\Phi = 1$. The important chemiluminescence signals from OH (309 nm) and CH (385 nm, 430 nm) can be seen, as well as the broadband signal from CO_2 (285 nm – 550 nm) and water represented by several bands above 690 nm [4, 5].
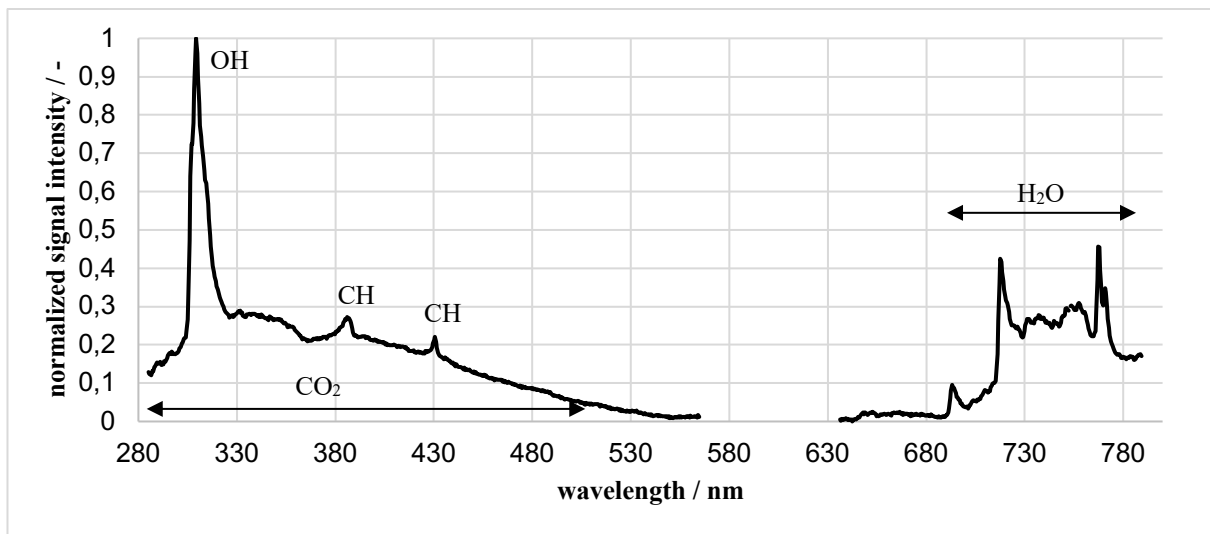

Fig.2: Determined emission spectrum (50.85 % hydrogen, fuel/air ratio $\Phi = 1$, time resolution 33 °KW).

The standard deviation of the OH and CH chemiluminescence signal intensities were used to investigate the stability of the combustion process at different operation points. The results show that a high amount of hydrogen in the reformate gas does not negatively affect the combustion stability. Changes of the EGR ratio also does not lead to changes of the combustion stability. However, an increase in the standard deviation has been observed for fuel/air ratios higher than 1, indicating an unstable combustion situation.

References

[1]   World Energy Outlook, 2019
[2]   B. Block, "Untersuchung von Möglichkeiten und Grenzen optischer Meßtechniken zur Temperaturbestimmung in Verbrennungsmotoren", PhD Thesis University of Hannover, Hannover, November 21, 1997.
[3]   S. Schlüter, T. Seeger, N. Popovska-Leipertz, A. Leipertz, "Laserbasierte On-line-Analyse von Biogasen mit einer Raman-Sonde", Tech. Mess., 81, 11, pp. 546–553, 2014.
[4]   T.F. Guiberti, D. Durox, T. Schuller, "Flame chemiluminescence from CO2- and N2-diluted laminar CH4/air premixed flames", Combust. Flame, 181, pp. 110-122, 2017.
[5]   R.W. Schefer, W.D. Kulatilaka, B.D. Patterson, T.B. Settersten, "Visible emission of hydrogen flames", Combust. Flame, 156, pp. 1234-1241, 2009.

Intra-Operative Registration of 2D C-Arm Images with Pre-Operative 3D CT-Scan Data in Computer Assisted Spine Surgery

Julio C. Alvarez-Gomez[1,2], Hubert Roth[1,2], and Jürgen Wahrburg[1,2]

(1) Center for Sensor Systems (ZESS), University of Siegen, D-57076 Siegen, Germany
(2) Institute of Control Engineering, University of Siegen, D-57076 Siegen, Germany
E-Mail: julio.agomez@uni-siegen.de Web: www.zess.uni-siegen.de/modicas;

Introduction

High-quality 3D pre-operative image devices such as CT-Scanners allow surgeons to plan surgical procedures. A significant challenge is how to bring the planning data to the operating scenario. CT-Scanners are usually in the radiology department; therefore, it is necessary to use 2D C-arms found in operating rooms to create a link between pre-operative data and the actual state of the patient. We present in this work an approach to register 3D pre-operative CT data using 2D images from a C-arm and an optical tracking system (OTS).

Materials and Methods - In 3D volumes obtained from the CT-scanner, elements like implants can be planned, i.e., their poses are determined within the DICOM coordinate system (DICOM_T_IMPLANT). During the surgical procedure, the patient has a rigid body (RB) attached to his body (ARB). Additionally, a RB attached to the C-arm detector head (CRB) is used to hold the C-ARM reference frame. The OTS tracks RBs and reports their poses, in this case, OTS_T_ARB and OTS_T_CRB. Fig.1 shows these reference frames. Moreover, our spine surgery robot has an RB attached to its end tool (TRB) trackable as OTS_T_TRB. Our final scope is to obtain the transformation from the robot tool to the position of the implants (TRB_T_IMPLANT). The focus of this work, nevertheless, is to bring the DICOM frame to the patient reference frame (DICOM_T_ARB).
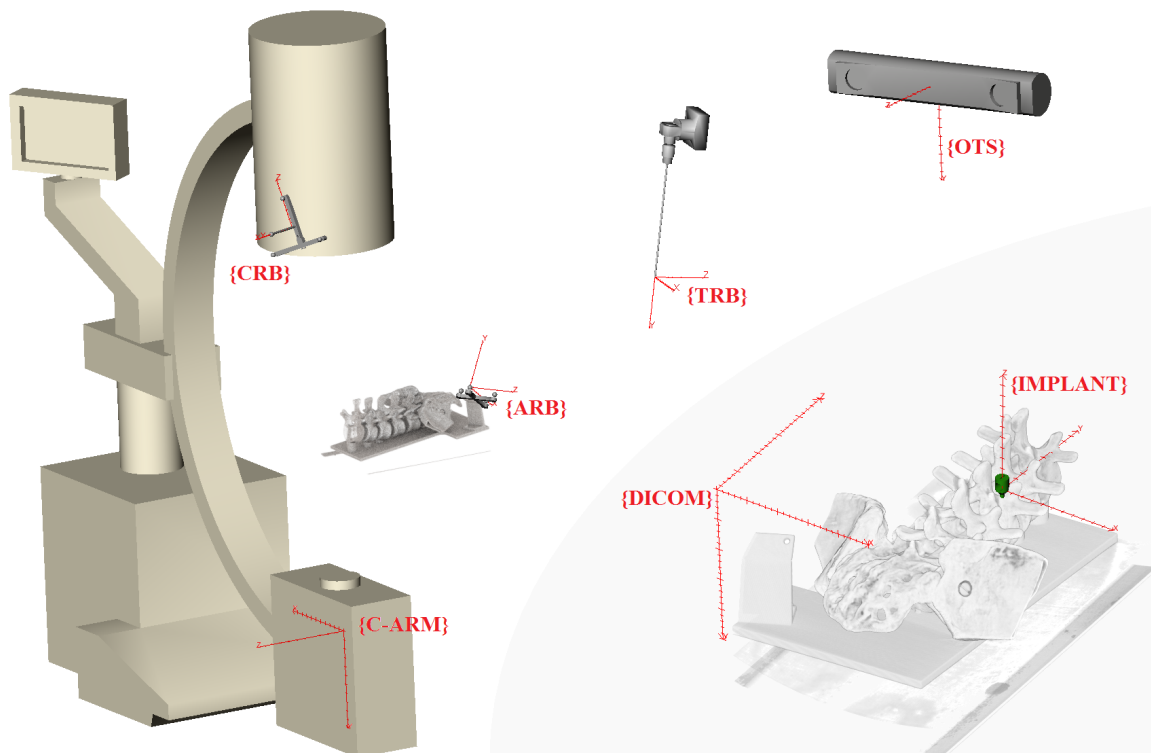

Fig.1: Intra- and pre-operative reference frames involved in the registration process

We implemented the 2D/3D registration procedure using an iterative intensity-based method [1]. The 2D input is a C-arm image, which is used as the set point for an optimization process, and the 3D input is a CT-Scan. A comparison is then executed in the R^2 space by projecting the CT-Scan into R^2 with a procedure called digitally reconstructed radiograph (DRR), which depends on the 6 DOF available in R^3 [2]. The DRR acts as a virtual C-arm whose coordinate frame center is located in the X-ray source. Likewise, we find the C-arm's origin using the pinhole camera model with the help of a calibration device attached to the detector [3]. The DRR and the C-arm images are compared using mutual information [4]. The result of the comparison is evaluated

by an optimization function that gives a new pose for the DRR. Once the registration finishes, the DRR and C-arm reference frames are considered the same (see Fig.2). In other words, the transformation CARM_T_DRR is the identity. This assumption makes it possible to compute the desired transformation DICOM_T_ARB.

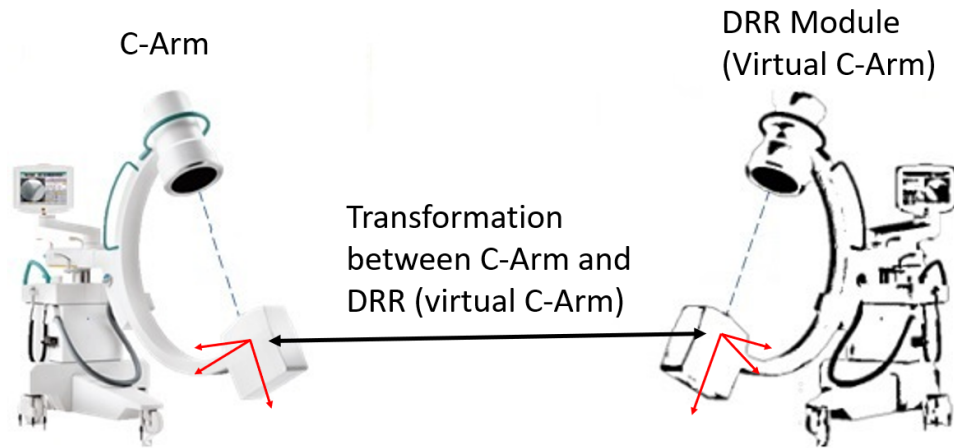*Fig.2: Transformation between C-Arm and DRR Modules*

Results - We carried out tests using two different phantoms from whom we took CT-Scans. One of them contains the sacrum and vertebrae L1 to L5. The second contains vertebrae L2 to L5. It is possible to use any projections for the registration, but the literature suggests to use perpendicular projected images [5]. Therefore, we use an anteroposterior and a lateral image. Then the registration process starts using the two radiographs and the pre-operative CT data. The planning data is transferred to the ARB after the registration ends. At this point, we used an adept surgical robot to perform the implant procedure. We report RMS errors of around ±2mm at this stage of our research. Regarding orientation, we have not implemented a setup to calculate the error in the angles accurately, so we do not make comments regarding angular accuracy.

Conclusions – We implemented a 2D/3D registration process from CT Data to intra-operative 2D C-arm images to facilitate the transfer of pre-operative 3D planning to intra-operative execution. With the help of an optical tracking system, a rigid body attached to the C-arm detector, and another to the patient, we manage to bring the CT volume to the patient state inside the operating theater. Using our phantoms and a spine surgery robot, we have achieved RMS errors of ±2mm.

References

[1]   S. Aouadi and L. Sarry, "Accurate and precise 2D–3D registration based on X-ray intensity," Computer Vision and Image Understanding, vol. 110, no. 1, pp. 134-151, 2008.

[2]   F. Jacobs, E. Sundermann, B. De Sutter, M. Christiaens, and I. Lemahieu, "A fast algorithm to calculate the exact radiological path through a pixel or voxel space," 1998.

[3]   R. Hartley and A. Zisserman, Multiple View Geometry in Computer Vision, 2nd ed., New York: Cambridge University Press, 2004.

[4]   Alvarez-Gomez J, Roth H, Wahrburg J.:"Comparison of Similarity Measurements and Optimizers for Intraoperative Registration of 2D C-arm Images with Preoperative CT Data in Computer-Assisted Spine Surgery." 18th Annual Meeting of the German Society for Computer- and Robot-Assisted Surgery. 2019.

[5]   G. Zheng, X. Zhang and L. Nolte, "Assessing Spline-Based Multi-resolution 2D-3D Image Registration for Practical Use in Surgical Guidance," Lecture Notes in Computer Science, vol. 3150, pp. 294-301, 2004.

IMPRESSUM

Editors:

Prof. Dr. Jörg Himmel, University of Applied Sciences Ruhr West
Prof. Dr. Daniel Erni, University of Duisburg Essen
Dipl. -Ing. (Univ.) Alice Fischerauer, University of Bayreuth
Prof. Dr. Olfa Kanoun, TU Chemnitz
Prof. Dr. Thomas Seeger, University of Siegen
Prof. Dr. Klaus Thelen, University of Applied Sciences Ruhr West

Scientific Advisory Board:

Prof. Dr. Gerhard Fischerauer, University of Bayreuth
Dipl. -Ing. (Univ.) Alice Fischerauer, University of Bayreuth
Prof. Dr. Jörg Himmel, University of Applied Sciences Ruhr West
Prof. Dr. Olfa Kanoun, Chemnitz University of Technology
Prof. Dr. Lothar Kempen, University of Applied Sciences Ruhr West
Prof. Dr. Frank Kreuder, University of Applied Sciences Ruhr West
Prof. Dr. Gennadij Lukjanow, ITMO University, St. Petersburg
Prof. Dr. Dirk Rüter, University of Applied Sciences Ruhr West
Prof. Dr. Thomas Seeger, University of Siegen
Prof. Dr. Olfa Kanoun, Chemnitz University of Technology
Prof. Dr. Klaus Thelen, University of Applied Sciences Ruhr West

Responsible according to German press law:

President of the University of Applied Sciences Ruhr West, Prof. Dr. Susanne Staude,
Duisburger Str. 100, 45479 Mülheim an der Ruhr

University of Applied Science Ruhr West
Duisburger Str. 100
45479 Mülheim an der Ruhr

ISBN: 978-3-946757-03-0

Print

University of Siegen
UniPrint
Hölderlinstr. 3
57076 Siegen
Print run: 100 pieces, as of June 2020

Legal disclaimer

Die Wiedergabe von Gebrauchsnamen, Handelsnamen, Warenbezeichnungen usw. in diesem Werk berechtigt auch ohne besondere Kennzeichnung nicht zu der Annahme, dass solche Namen im Sinne der Warenzeichen- und Markenschutz-Gesetzgebung als frei zu betrachten wären und daher von jedermann benutzt werden dürften.

Sollte in diesem Werk direkt oder indirekt auf Gesetze, Vorschriften oder Richtlinien (z. B. DIN, VDI, VDE) Bezug genommen oder aus ihnen zitiert worden sein, so kann die Hochschule keine Gewähr für Richtigkeit, Vollständigkeit oder Aktualität übernehmen. Es empfiehlt sich, gegebenenfalls für die eigenen Arbeiten die vollständigen Vorschriften oder Richtlinien in der jeweils gültigen Fassung hinzuzuziehen.

Für Titel und Inhalt der Präsentation ist der jeweilige Verfasser selbst verantwortlich.

Mülheim an der Ruhr, August 2020

With generous support from:

FÖRDERVEREIN DER
HOCHSCHULE RUHR WEST

WWW.HOCHSCHULE-RUHR-WEST.DE

HOCHSCHULE RUHR WEST
UNIVERSITY OF APPLIED SCIENCES